nature materials

Article

https://doi.org/10.1038/s41563-025-02295-7

Computational design of bifaceted protein nanomaterials

Received: 20 December 2024

Accepted: 18 June 2025

Published online: 31 July 2025

Check for updates

Sanela Rankovic[1,2], Kenneth D. Carr[1,2], Justin Decarreau[1,2], Rebecca Skotheim[1,2], Ryan D. Kibler[1,2], Sebastian Ols[1,2], Sangmin Lee[1,2], Jung-Ho Chun[1,2], Marti R. Tooley[1,2], Justas Dauparas[1,2], Helen E. Eisenach[1,2], Matthias Glögl[1,2], Connor Weidle[1,2], Andrew J. Borst[1,2], David Baker[1,2,3] & Neil P. King[1,2] ✉

Advances in computational methods have led to considerable progress in the design of protein nanomaterials. However, nearly all nanoparticles designed so far exhibit strict point group symmetry, which limits structural diversity and precludes anisotropic functionalization. Here we describe a computational strategy for designing multicomponent bifaceted protein nanomaterials with two distinctly addressable sides. The method centres on docking pseudosymmetric hetero-oligomeric building blocks in architectures with dihedral symmetry and designing an asymmetric protein–protein interface between them. We obtain an initial 30-subunit assembly with pseudo-D_5 symmetry and generate variants in which we alter the size and morphology of the bifaceted nanoparticles by designing extensions to one of the subunits. Functionalization of the two nanoparticle faces with protein minibinders enables the specific colocalization of two populations of polystyrene microparticles coated with the target protein receptors. The ability to accurately design anisotropic protein nanoparticles could be broadly useful in applications requiring the colocalization of distinct target moieties.

Multi-subunit protein complexes are fundamental for nearly all biological processes and have inspired efforts to design new self-assembling proteins[1–4]. Computationally designed protein nanoparticles have emerged as a promising class of nanomaterials that have served as robust scaffolds for a number of applications, encompassing multivalent antigen presentation[5–11], structure determination[12–14], enzyme colocalization[15], and enhancement of receptor-mediated signalling and virus neutralization[16–18]. Most of the computationally designed nanoparticles described so far have been constructed using a dock-and-design approach in which symmetric building blocks are docked together in a target architecture, and then low-energy protein–protein interfaces are designed between the building blocks to drive assembly[5,19–22]. This approach is efficient in that it allows the construction of large structures from a small number of subunits and minimizes the number of novel protein–protein interfaces that must be designed[3,23]. However, it also constrains the sizes, shapes and symmetries of the assemblies that can be designed, limiting their functionalization and application. Recent methodological advances have led to the emergence of a novel approach based on the design of pseudosymmetric hetero-oligomers in which subunits with identical backbone structures but distinct amino acid sequences are arranged symmetrically (for example, as trimers)[24]. These building blocks allowed the extension of the dock-and-design approach to the construction of very large pseudosymmetric protein nanoparticles through the incorporation of several designed protein–protein interfaces in a single material[25,26]. Nonetheless, even these pseudosymmetric nanoparticles have global tetrahedral, octahedral or icosahedral point group symmetry and, as a result, isotropically distributed subunits across their entire surfaces. Moving beyond

[1]Department of Biochemistry, University of Washington, Seattle, WA, USA. [2]Institute for Protein Design, University of Washington, Seattle, WA, USA. [3]Howard Hughes Medical Institute, University of Washington, Seattle, WA, USA. ✉e-mail: neilking@uw.edu

https://doi.org/10.1038/s41563-025-02295-7

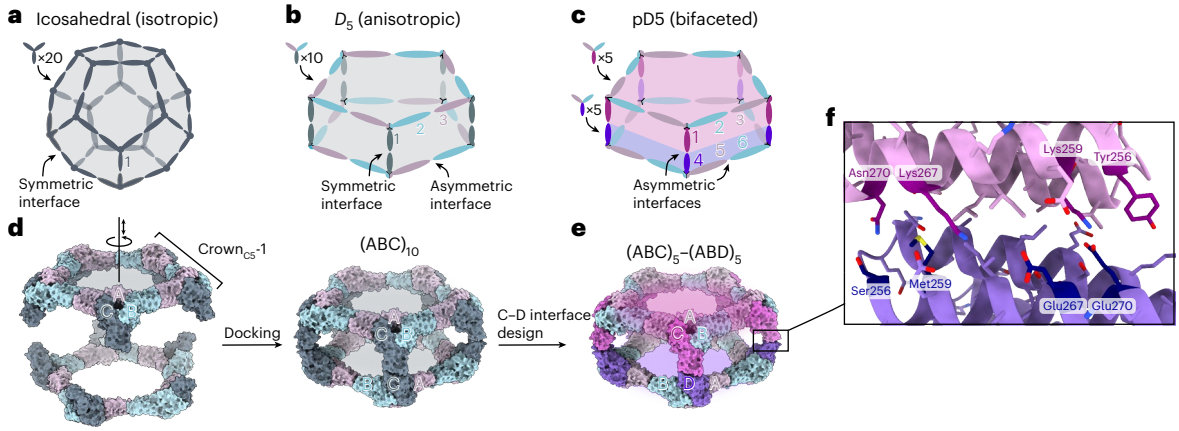

Fig. 1 | Overview of bifaceted pD5 architecture and design approach. **a**, A nanoparticle with icosahedral symmetry constructed from homotrimeric building blocks requires only a single (symmetric) designed interface and is isotropic overall. **b**, A nanoparticle with dihedral symmetry (D_n; in this example, $n = 5$) constructed from a single heterotrimeric building block requires two designed interfaces: an asymmetric interface around the n-fold symmetry axis and a symmetric interface along the dihedral two-fold axes. The assembly is anisotropic, but the two opposing faces are constructed from the same three subunits (labelled 1, 2 and 3) and are not independently addressable. **c**, An anisotropic D_n assembly can be converted to a bifaceted pseudo-D_n assembly by asymmetrizing the designed interface at the dihedral two-fold axes. The nanoparticle is constructed from two different heterotrimers that can be produced independently before nanoparticle assembly, rendering each of the six subunits uniquely addressable, even if subunits 2 + 6 and 3 + 5 are genetically identical. **d**, Schematic of the procedure for docking Crown$_{C5}$-1 substructures into (ABC)$_{10}$ assemblies with D_5 symmetry. The A, B and C subunits of Crown$_{C5}$-1 are labelled, and the rotational and translational degrees of freedom sampled during docking are indicated along the five-fold symmetry axis. **e**, An example bifaceted (ABC)$_5$–(ABD)$_5$ assembly after asymmetric C–D interface design. **f**, Details of an example asymmetric C–D interface. Positions featuring different amino acids in the C and D subunits are highlighted.

isotropic materials to those with controllable anisotropy or directionality requires design methods that incorporate additional asymmetry.

Bifaceted or Janus-like architectures are one such class of anisotropic nanomaterials[27]. Their defining feature is two distinct faces composed of unique molecules that are independently addressable. This property makes Janus-like particles particularly useful in applications that require bringing two different entities together. For example, bispecific T cell engagers are a simple and clinically relevant class of such molecules in which a genetic fusion of two different single-chain variable fragments, one against a T cell marker and the other against a tumour-associated antigen, enhances the anticancer activity of T cells by colocalizing them with tumour cells[28]. Self-assembling bifaceted materials have been constructed from a wide range of materials, including metals, silicon dioxide, titanium dioxide, graphene, polyethylene, polystyrene, polyacrylic acid, lipids and DNA[29–31]. In particular, DNA nanotechnology has been used to construct Janus-like particles that improve cancer vaccination and enhance endosomal escape[30,32]. The design of bifaceted nanoparticles from protein building blocks would be particularly useful due to their multivalency, biocompatibility, modular functionalization through genetic fusion or conjugation of functional domains, and the potential to controllably alter their structures with atom-level accuracy. Despite this potential, methods for accurately designing bifaceted protein nanomaterials have not yet been developed.

Here we develop a general computational approach that enables the design of pseudosymmetric bifaceted protein nanoparticles with precisely tunable structures. We found that displaying protein minibinders on the opposing faces of one such structure enabled it to specifically colocalize polystyrene microparticles coated with therapeutically relevant target proteins, highlighting the potential biomedical utility of this novel class of self-assembling proteins.

Results

Computational design of bifaceted D_5 protein nanomaterials

Designing isotropic protein nanomaterials from oligomeric building blocks minimally requires only a single designed protein–protein interface (Fig. 1a), a principle that has been previously leveraged to design a wide variety of novel self-assembling proteins[19,23,33,34]. By contrast, multiple distinct protein–protein interfaces are required to construct anisotropic and bifaceted protein complexes. For example, anisotropic assemblies with D_5 symmetry could be constructed from heterotrimeric building blocks by combining (1) an asymmetric interface that gives rise to global five-fold rotational symmetry with (2) a symmetric interface along the five dihedral symmetry axes (Fig. 1b). In this architecture, each of the three subunits of the heterotrimeric building block is genetically distinct and, therefore, independently addressable, but the two sides of the overall assembly cannot be uniquely addressed because the trimers would self-assemble. However, if the dihedral interface is instead asymmetric, the resultant pseudo-D_5 (pD5) complexes could not assemble until two different heterotrimers are mixed, yielding bifaceted nanomaterials in which each of the six independent subunits could be uniquely functionalized (Fig. 1c). We refer to this pD5 architecture as (ABC)$_5$–(ABD)$_5$ to indicate its bifaceted nature and hierarchical assembly from heterotrimeric building blocks.

We recently showed that stepwise approaches facilitate the design of self-assembling protein complexes featuring multiple designed interfaces[24–26]. To design bifaceted pD5 nanoparticles, we leveraged a 15-subunit substructure of a recently described pseudosymmetric icosahedral assembly[25]. This ring-like substructure, called Crown$_{C5}$-1, comprises five copies of a pseudosymmetric trimer with three-fold symmetry at the backbone level but distinct amino acid sequences for each subunit ('ABC' heterotrimers). A previously designed interface between the A and B chains drives the assembly of the heterotrimers into the 15-subunit substructure with five-fold rotational symmetry, leaving the C-terminal end of the C subunits free for the design of an additional interface. We docked two full-length Crown$_{C5}$-1 assemblies against each other by sampling the rotation and translation along the five-fold axis to generate 30-subunit assemblies with D_5 symmetry (Fig. 1d). To generate additional diversity, we also docked Crown$_{C5}$-1 models in which the C terminus of the C subunit was truncated by up to four α-helices. We then used ProteinMPNN[35] to design an asymmetric protein–protein interface between the opposing C subunits of each dock to generate sequences intended to form bifaceted (ABC)$_5$–(ABD)$_5$ complexes (Fig. 1e). We used several negative-design strategies during

asymmetric interface design by (1) biasing ProteinMPNN to favour residues of opposite charge, size or both on the two sides of the C–D interface or (2) performing explicit multistate design to select residues that stabilize the on-target interface and destabilize potential off-target C–C or D–D interfaces (Methods)[35,36]. These approaches yielded interfaces in which a subset of symmetry-related positions featured distinct amino acids on the C and D subunits (Fig. 1f).

We used AlphaFold2 (AF2) structure prediction[37] of the five C-terminal helices of the C and D subunits to identify sequences strongly predicted to form the on-target C–D interface but not forming off-target C–C and D–D interfaces. Designs for which (1) the AF2 prediction of the C–D interface was within 2.0-Å Cα root mean square deviation (r.m.s.d.) from the design model, (2) mean predicted aligned error (pAE) for the interchain interactions (mean pAE interaction) was lower than 10 and (3) predicted local distance difference test (pLDDT) was higher than 90 were considered further (Extended Data Fig. 1a). Out of these, we discarded designs for which the structure prediction of either of the off-target C–C or D–D interfaces yielded r.m.s.d. < 2.0 Å, mean pAE interaction < 10 and pLDDT > 95 (Extended Data Fig. 1b). To further filter for asymmetry-favouring sequences, we identified designs in which the difference in the mean pAE interaction between the C–D and either C–C or D–D interfaces was greater than 10. Biasing ProteinMPNN to favour residues of opposite charge or opposite charge and size across the C–D interface generated the most designs that passed these criteria. We selected 14 designs from these two groups for experimental characterization, as well as all seven passing designs from a set in which ProteinMPNN was used with no negative-design considerations. The amino acid sequences of all the novel proteins generated in this study are provided in Supplementary Table 1.

Experimental characterization of bifaceted pD5 nanoparticles

We expressed the A, B, C and D subunits for each design separately in *Escherichia coli* (with a 6×His tag on the A component), mixed the cells from the A + B + C and A + B + D expression bacterial cultures before lysis, and purified the proteins from clarified lysates as cyclic $(ABC)_5$ and $(ABD)_5$ assemblies using immobilized metal affinity chromatography (IMAC) and size exclusion chromatography (SEC). Despite our negative-design strategies, SEC and negative-stain electron microscopy (nsEM) showed that nearly all of the designs formed off-target assemblies: 4 yielded either an $(ABC)_{10}$ or $(ABD)_{10}$ assembly, whereas 16 yielded both $(ABC)_{10}$ and $(ABD)_{10}$ assemblies. These results probably reflect the tendency of even modest protein–protein interactions to drive the association of high-symmetry building blocks[38,39]. One design from the set biased to favour residues of opposite charge and size across the C–D interface, called pD5-14, yielded cyclic $(ABC)_5$ and $(ABD)_5$ assemblies that did not form off-target $(ABC)_{10}$ or $(ABD)_{10}$ assemblies but yielded an earlier elution peak during SEC when mixed, suggesting the formation of a larger assembly (Fig. 2a). Sodium dodecyl sulfate–polyacrylamide gel electrophoresis (SDS-PAGE) of the peak fraction indicated the presence of all four components in the shifted peak, and additionally revealed the presence of an unexpected band just under 50 kDa in the $(ABC)_5$ and $(ABC)_5$–$(ABD)_5$ preparations (Fig. 2b). On the basis of the size of this band and the observation of small numbers of compact, apparently octahedral particles during nsEM, we suggest that this band corresponds to dihydrolipoamide succinyltransferase, a commonly observed contaminant from *E. coli* host cells[40]. Dynamic light scattering (DLS) and mass photometry (MP)[41] of the $(ABC)_5$–$(ABD)_5$ preparations showed the existence of particles measuring approximately 25.1 nm in size and 1,151 kDa in mass, respectively, closely matching the expected values for the target bifaceted nanoparticle (Extended Data Fig. 2a,b). Ring-like structures resembling $Crown_{C5}$-1 were observed during nsEM of the pD5-14 $(ABC)_5$ and $(ABD)_5$ components as expected, along with a substantial fraction of unassembled heterotrimeric building blocks (Fig. 2c,d). By contrast, electron micrographs of the purified pD5-14 $(ABC)_5$–$(ABD)_5$ complexes revealed monodisperse fields of particles that resembled the intended 30-subunit structure, with considerably fewer unassembled heterotrimers (Fig. 2e). Rigid-body fits of the pD5-14 $(ABC)_5$, $(ABD)_5$ and $(ABC)_5$–$(ABD)_5$ design models into the corresponding low-resolution three-dimensional (3D) reconstructions strongly suggested that each assembly adopted the intended structure. The $(ABC)_5$–$(ABD)_5$ complexes were remarkably thermostable: essentially, no changes in hydrodynamic diameter, intrinsic tryptophan fluorescence or static light scattering were observed as the pD5-14 complexes were heated from 25 °C to 95 °C, indicating that the assemblies do not unfold or aggregate even when subjected to near-boiling temperatures (Extended Data Fig. 2c–e).

To evaluate the accuracy of our design approach at higher resolution, the pD5-14 $(ABC)_5$–$(ABD)_5$ sample was vitrified and imaged using cryo-electron microscopy (cryo-EM; Extended Data Fig. 3a). Two-dimensional (2D) class averages clearly indicated the formation of particles with the intended morphology (Fig. 2f and Extended Data Fig. 3b), and a single-particle reconstruction using C_5 symmetry resulted in a 4.30-Å volume map in which individual α-helices were well resolved (Fig. 2g and Extended Data Fig. 3c–f). Relaxing the helices of the pD5-14 design model into the cryo-EM density resulted in a structure that matched the design model remarkably well, yielding a backbone r.m.s.d. of 3.0 Å over the entire 30-subunit assembly. Aligning only the two subunits comprising the asymmetric C–D interface yielded a backbone r.m.s.d. of 1.3 Å, although we could not distinguish the C and D chains from each other since the side chains were not resolved (Fig. 2h). Overall, our cryo-EM analysis of pD5-14 $(ABC)_5$–$(ABD)_5$ complexes assembled in vitro confirmed that our approach enables the design of bifaceted protein nanomaterials with high accuracy.

Fine tuning of bifaceted pD5 nanoparticle size and shape

Many biological phenomena, including T cell activation, synaptic transmission and exocytosis, strongly depend on the distance between two biological objects such as cells or secretory vesicles[42–44]. However, methods or tools for bringing two entities together at prescribed distances are still lacking. We leveraged the recently developed machine learning-based design tools RFdiffusion[45] and ProteinMPNN[35] to design bifaceted nanomaterials with systematically varying size and shape by generating de novo extensions within the C subunit of pD5-14. Specifically, we 'cut' the loop preceding the last two helices of the C subunit to leave the asymmetric C–D interface intact and translated the remainder of the $(ABC)_5$ substructure 25 Å, 50 Å, 75 Å and 100 Å along the five-fold axis (Fig. 3a). We defined an additional target in which we translated the $(ABC)_5$ substructure 50 Å and also rotated it 25°. For each target structure, we used RFdiffusion to generate a de novo protein backbone connecting the translated portion of the C subunit to its interface-forming C-terminal helices, designed amino acid sequences for the de novo extensions using ProteinMPNN and predicted the structures of the designed C subunits using AF2 (Fig. 3b). The number of residues making up the de novo extensions in designs that passed our AF2 filters (pLDDT > 90 and r.m.s.d. to the RFdiffusion output < 1.5 Å) differed between each target architecture (Fig. 3c). For example, passing designs for the 25-Å extension were narrowly distributed around 75 inserted amino acids, whereas 300–400 inserted amino acids were required for the 100-Å extensions. The de novo backbones generated by RFdiffusion were often helical repeats that resembled the topology of the original subunit, and inserting more diffused residues for a given extension generally led to an additional α-helix or occasionally extruded loops (Extended Data Fig. 4a). Interestingly, a higher proportion of backbones comprising β-sheets was observed for the 75-Å and 100-Å extensions, but none of these designs passed our AF2 filters (Extended Data Fig. 4b). We selected for the experimental characterization of the designs with the lowest r.m.s.d. values between their AF2 predictions and diffused backbones, comprising 7 designs for the 25-Å extension and 10 each for the 50-Å, 75-Å and 100-Å extensions as well as the 50-Å extension with a 25° rotation.

https://doi.org/10.1038/s41563-025-02295-7

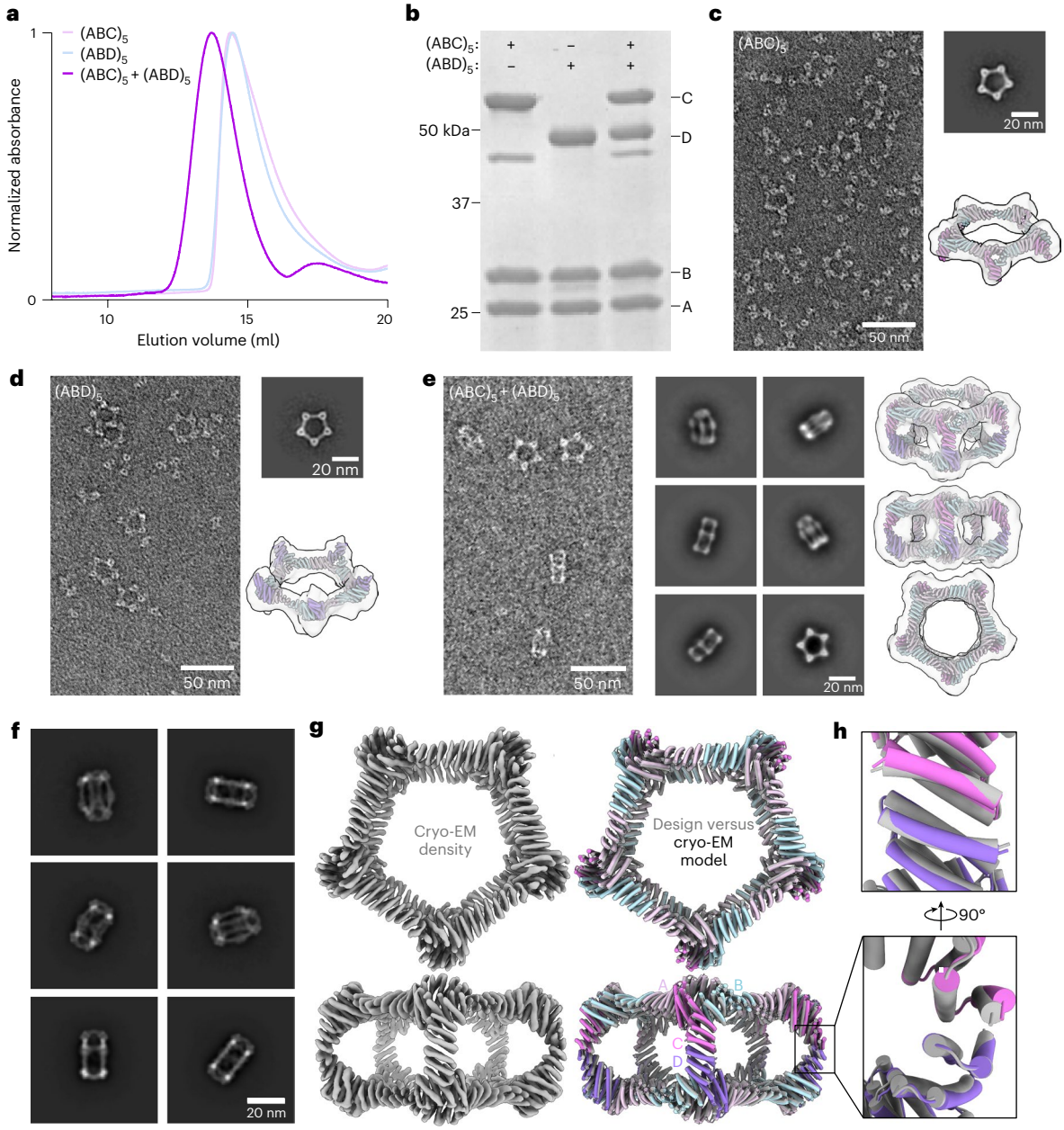

Fig. 2 | In vitro assembly and structural characterization of pD5-14. a, SEC traces of pD5-14 $(ABC)_5$, $(ABD)_5$ and $(ABC)_5$–$(ABD)_5$ assemblies. **b**, SDS-PAGE of SEC-purified assemblies from **a**. The locations of the A, B, C and D subunits, as well as those of marker bands, are indicated. **c**–**e**, nsEM of pD5-14 $(ABC)_5$ (**c**), $(ABD)_5$ (**d**) and $(ABC)_5$–$(ABD)_5$ (**e**) assemblies, including representative 2D class averages and rigid-body fits of the computational design models into 3D reconstructions. **f**, Cryo-EM 2D class averages of pD5-14 $(ABC)_5$–$(ABD)_5$. **g**, Left: 4.30-Å-resolution cryo-EM density map of pD5-14 $(ABC)_5$–$(ABD)_5$ viewed along two orthogonal axes. Right: overlay between the computational design model (grey) and the experimentally determined cryo-EM model (colours). **h**, Details of asymmetrically designed C–D interface. Scale bars, 50 nm (raw micrographs); 20 nm (2D class averages).

We expressed and purified each new $(ABC)_5$ design as described above, mixed them with pD5-14 $(ABD)_5$ and assessed pD5 particle formation by SEC (Extended Data Figs. 5 and 6). We observed peaks at the expected elution volumes for two to four of the designs from each of the extended architectures (Supplementary Table 1). The SEC traces also indicated that in all cases, a substantial portion of each mixture remained as unassembled $(ABC)_5$ and $(ABD)_5$ components. Three of the four successful designs extended by 100 Å were derived from the same RFdiffusion-generated backbone and differed only at the sequence level ($pD5_{+100}$-46, $pD5_{+100}$-48 and $pD5_{+100}$-71). As with pD5-14, nsEM showed that each extended $(ABC)_5$ component before mixing with $(ABD)_5$ formed only ring-like substructures resembling $Crown_{C5}$-1, with substantial amounts of unassembled trimers also present (Fig. 4 and Extended Data Fig. 6). By contrast, after mixing with pD5-14 $(ABD)_5$, D_5-like assemblies with aspect ratios clearly different from pD5-14 were the predominant species, with some unassembled trimers present, too. These unassembled trimers may be derived from the $(ABC)_5$ or $(ABD)_5$ assemblies that were not fully separated by SEC and subsequently disassembled during nsEM grid preparation. Although 2D class averages of particles extended by 25 Å, 50 Å, 75 Å and 100 Å each strongly resembled the five-pointed star of pD5-14 viewed along its five-fold symmetry axis, the averages of $pD5_{+50/25°}$-344 uniquely showed two lobes at each of the five points, consistent with the designed 25° rotation. Low-resolution single-particle reconstructions of one assembly of each type confirmed that they adopted the intended structures, including the 'bent' pillars connecting the two distinct faces of $pD5_{+50/25°}$-344.

https://doi.org/10.1038/s41563-025-02295-7

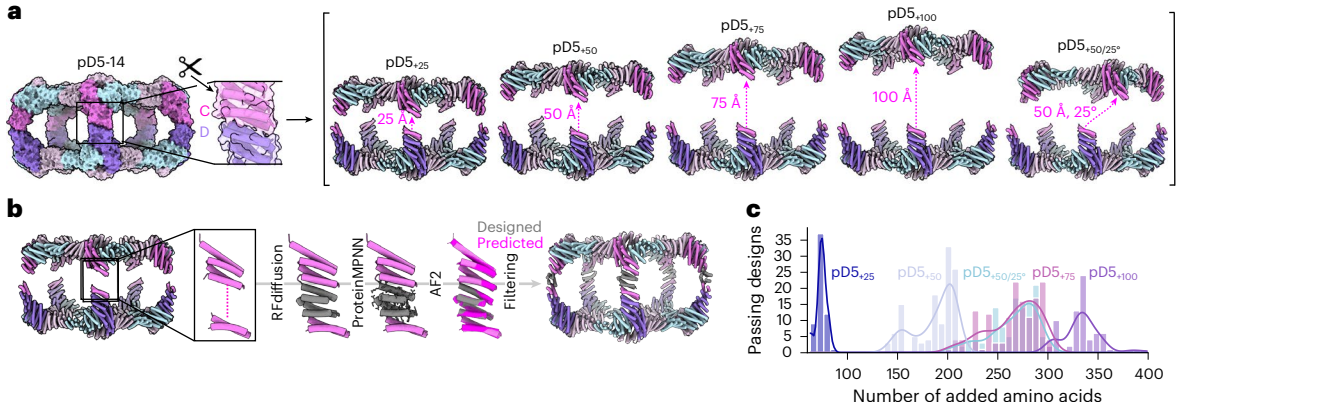

Fig. 3 | Fine tuning of bifaceted protein nanoparticle size and shape using RFdiffusion. a, Schematic of the approach used to define target extended architectures. Left: the scissors indicate the loop in the C subunit that was 'cut'. Right: target architectures were defined by translating and in one case rotating most of the $(ABC)_5$ substructure, leaving the designed asymmetric C–D interface intact. **b**, Schematic of the design process used to generate de novo C subunits for each extended architecture. **c**, Number of designs that passed AF2 filtering (pLDDT > 90; r.m.s.d. to design model < 1.5 Å) per number of added amino acid residues for each extended architecture.

DLS data of one representative assembly from each extended architecture further confirmed the size and monodispersity of the assemblies in solution (Extended Data Fig. 7). These data establish that our computational approach can accurately generate bifaceted protein nanomaterials with precisely tunable structures.

Bifaceted nanoparticles colocalize distinct microparticles

To demonstrate the ability of the bifaceted nanoparticles to colocalize two distinct entities, we sought to genetically fuse different de novo protein minibinders[46,47] to the subunits making up each face of pD5-14. However, neither terminus of any subunit was initially available for genetic fusion, as all the C termini were involved in the protein–protein interfaces that drive bifaceted nanoparticle assembly and the N termini were oriented towards the nanoparticle interior. We, therefore, redesigned the first three helices in all the subunits of pD5-14—which were identical at the backbone level—to generate new, outward-facing N termini. Specifically, we used block adjacency matrices in RFdiffusion, which enable the precise definition of target topologies and contacts[45] to (1) change the order of the first three helices, (2) insert a new α-helix to effect the desired change in directionality and (3) construct new loops between the redesigned helices (Fig. 5a). We generated 100 novel protein backbones, designed sequences for them using ProteinMPNN and filtered the designs using AF2 prediction. For experimental characterization, we selected ten designs with pLDTT > 90 and the lowest predicted r.m.s.d. to the original heterotrimer.

Two of the designs, namely, pD5-14_rd47 and pD5-14_rd106, yielded SEC peaks at the retention volume expected for the target bifaceted nanoparticle after mixing the redesigned $(ABC)_5$ and $(ABD)_5$ components (Extended Data Figs. 8a,b and 9a,b). Analysis of the SEC-purified assemblies by DLS indicated the existence of uniform particles of the expected size (~25 nm; Extended Data Figs. 8c and 9c). As before, nsEM of the separate $(ABC)_5$ and $(ABD)_5$ components showed only ring-like substructures and unassembled trimers, whereas the analysis of purified pD5-14_rd47 and pD5-14_rd106 $(ABC)_5$–$(ABD)_5$ assemblies yielded 2D class averages and 3D reconstructions that matched the size and morphology of the respective bifaceted nanoparticle design models (Extended Data Figs. 8d and 9d).

We made genetic fusions of the IL-2Rβ-targeting minibinder Neo-2/15 (ref. 46) and the 4-1BB-targeting minibinder 41bb_mb1 (ref. 48) to the redesigned pD5-14_rd47 B subunit and purified Neo-2/15-bearing $(ABC)_5$ and 41bb_mb1-bearing $(ABD)_5$ components, as described above. After mixing, SEC and nsEM confirmed the formation of the expected bifaceted nanoparticle, although the displayed minibinders could not be visualized due to their small size and the flexible genetic linker used (Fig. 5b,c). The dual-functionalized nanoparticle bound both IL-2Rβ and 4-1BB in biolayer interferometry (BLI) studies, whereas control bifaceted nanoparticles displaying only one of the two minibinders or the same minibinder on both faces (Extended Data Fig. 10) strongly bound the cognate receptor and only minimally binding the non-cognate receptor (Fig. 5d).

We then used the minibinder-displaying pD5-14_rd47 complexes to colocalize two distinct populations of fluorescent polystyrene microparticles. We first coated the microparticles with target receptors by separately conjugating biotinylated 4-1BB and IL-2Rβ to streptavidin-coated Nile Red-labelled and fluorescent-purple-labelled microparticles, respectively. After mixing the two microparticle populations and incubating them with unfunctionalized ('bare') pD5-14_rd47, control bifaceted nanoparticles displaying the same binder on both faces or the bifaceted nanoparticle displaying the two different binders on opposing faces, we measured colocalization using flow cytometry and fluorescence microscopy. Incubation with bare pD5-14_rd47 did not increase colocalization above background levels by flow cytometry (0.4%), whereas incubation with bifaceted nanoparticles displaying Neo-2/15 or 41bb_mb1 on both sides led to slightly increased numbers of double-positive events (1.4% and 1%, respectively; Fig. 5e,f), which may derive from the modest non-specific binding observed by BLI (Fig. 5d). By contrast, incubation with the bifunctionalized nanoparticle significantly increased the number of double-positive events (6.9%), indicating that displaying different protein minibinders on the two faces of pD5-14_rd47 efficiently colocalized the two populations of microparticles. Similar results were obtained by fluorescence microscopy, where 9.0% of the visualized microparticles were colocalized by the bifunctionalized nanoparticles, compared with 1.2%–2.4% colocalization after incubation with the three control nanoparticles (Fig. 5g). These data establish that our computationally designed bifaceted nanoparticles can be functionalized to colocalize two distinct biological entities.

Discussion

Our results establish a general computational approach for accurately designing bifaceted protein nanomaterials with customizable structures. Breaking symmetry is a current focus of innovation in the computational design of novel self-assembling proteins, as it simultaneously provides a route to much larger materials and unlocks the ability to address and functionalize specific locations (for example, subunits). A pair of recent reports from our groups used

https://doi.org/10.1038/s41563-025-02295-7

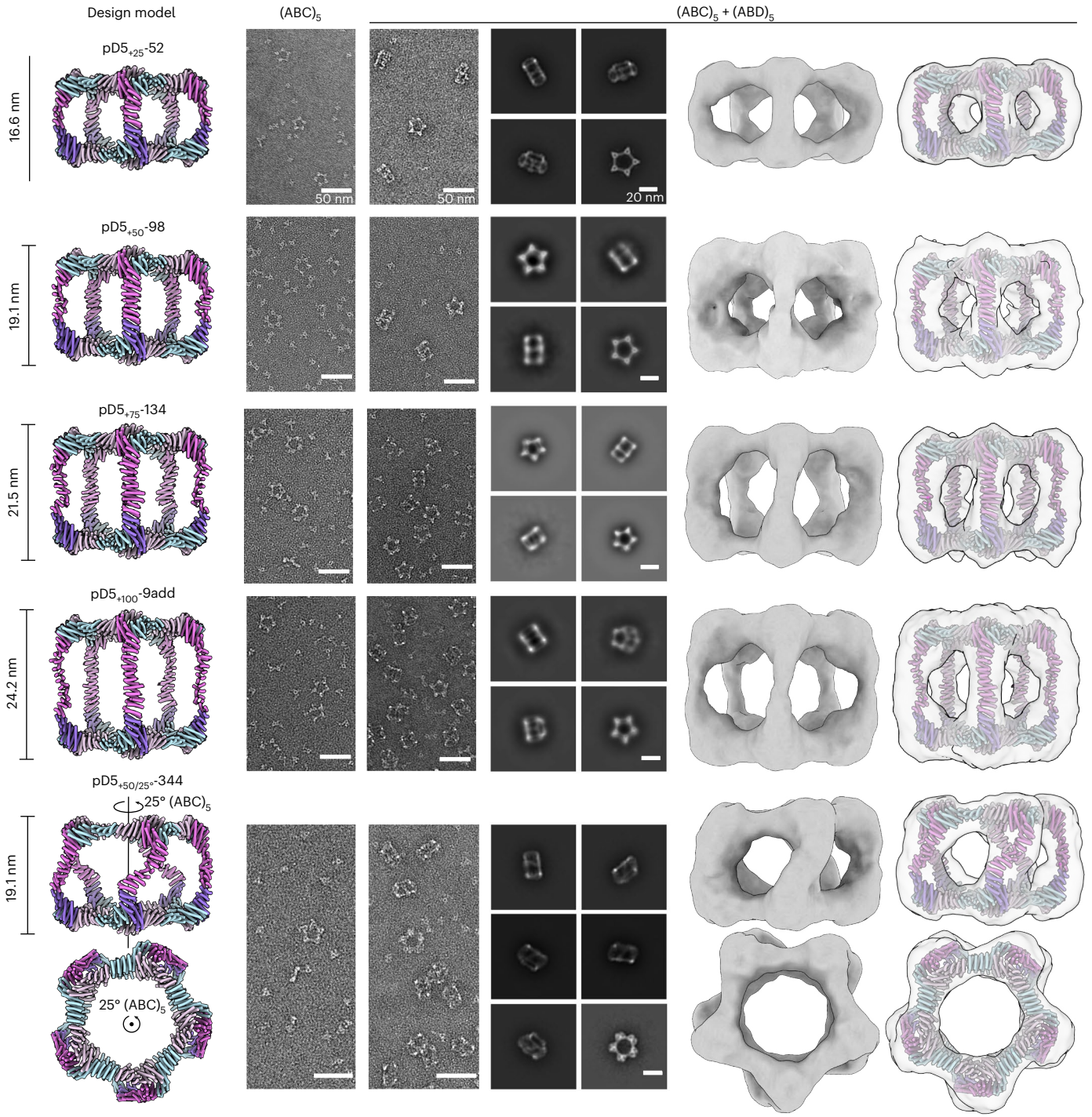

Fig. 4 | nsEM characterization of extended $(ABC)_5$–$(ABD)_5$ nanoparticles. From top to bottom: representative assemblies extended by 25 Å, 50 Å, 75 Å and 100 Å, or extended by 50 Å and rotated by 25°. From left to right: computational design models, raw micrographs of $(ABC)_5$, raw micrographs of $(ABC)_5$ + $(ABD)_5$, 2D class averages of $(ABC)_5$ + $(ABD)_5$ showing representative top and side views, 3D reconstructions and design models fit into the 3D reconstructions. Side views of the design models and 3D reconstructions are shown for each particle, except for $pD5_{+50/25°}$-344, for which the side and top views are shown. Scale bars, 50 nm (raw micrographs); 20 nm (2D class averages).

pseudosymmetric hetero-oligomeric building blocks[24] to build very large protein assemblies[36,49], yet these were still isotropic and, therefore, had limited addressability. Here we go beyond those strategies by designing anisotropic assemblies with two distinctly addressable faces. We are aware of only one previous report of an engineered multivalent Janus-like protein nanoparticle. In that study, mutations were introduced into a naturally occurring D_5 assembly (*Brucella* lumazine synthase) that disfavoured pentamer homodimerization and favoured pentamer heterodimerization[50]. Here we generated bifaceted nanoparticle architectures with target structural features by combining protein–protein docking, asymmetric interface design and generative design of de novo subunits. The pseudosymmetric, 30-subunit bifaceted nanoparticles we described do not, to our knowledge, resemble any known naturally occurring or engineered protein complexes. A limitation of the present study is that we only demonstrated the design of assemblies with pD5 symmetry. However, as demonstrated by the

https://doi.org/10.1038/s41563-025-02295-7

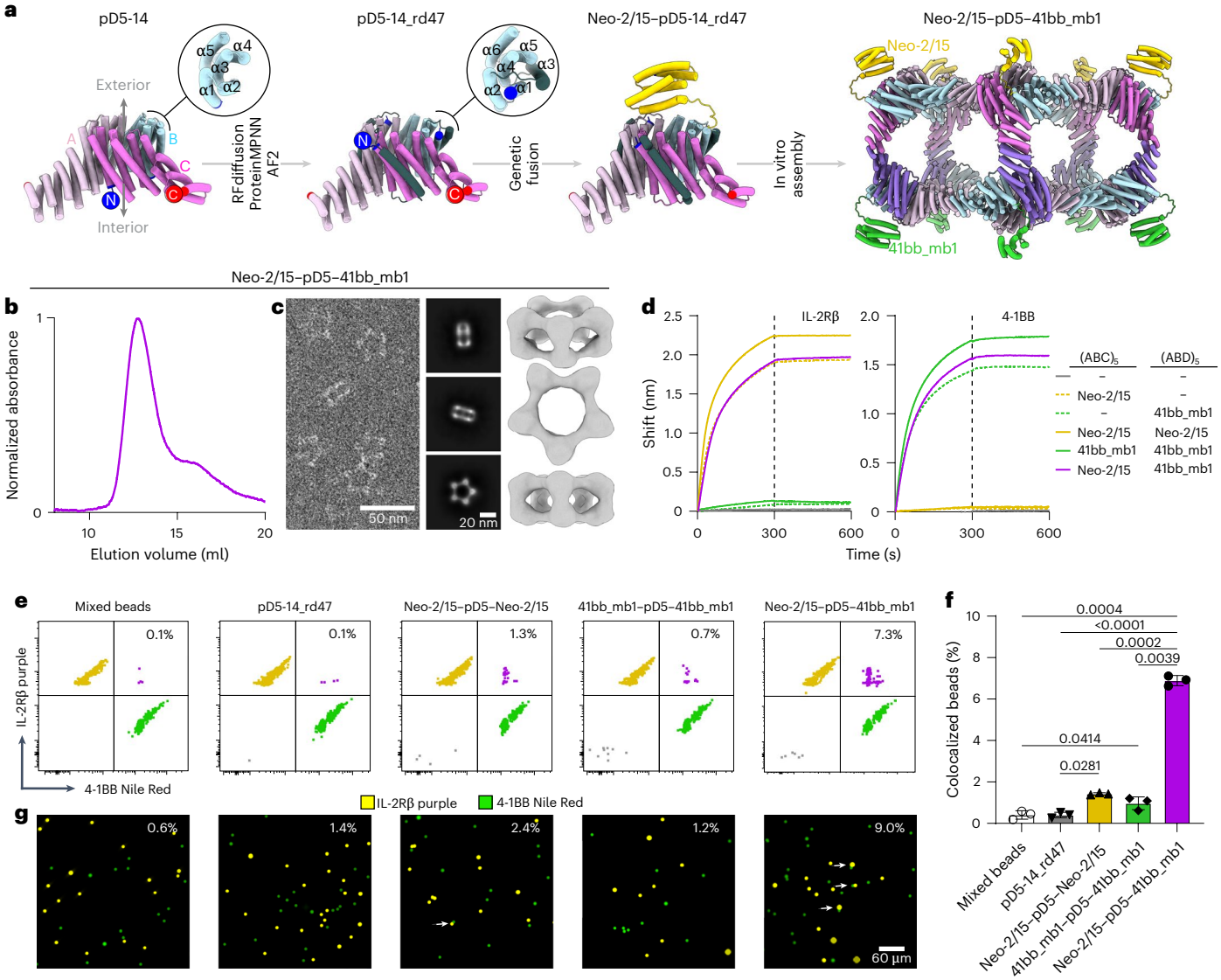

Fig. 5 | Minibinder-functionalized bifaceted nanoparticles colocalize two distinct fluorescent polystyrene microparticle populations. a, Schematic of the approach used to (1) reorient the N termini of the A, B and C subunits of pD5-14 to face towards the nanoparticle exterior and (2) independently functionalize each face of the resultant bifaceted nanoparticle with protein minibinders. The newly diffused α-helix is shown in dark grey, and the N and C termini are indicated by blue and red circles, respectively. **b**,**c**, SEC trace (**b**) and nsEM (**c**) of pD5-14_rd47 with Neo-2/15 and 41bb_mb1 genetically fused to the B components of the $(ABC)_5$ and $(ABD)_5$ components, respectively. Scale bars, 50 nm (raw micrograph); 20 nm (2D class averages). **d**, Binding of functionalized bifaceted nanoparticles to IL-2Rβ (left) and 4-1BB (right) ectodomains, measured by BLI. The legend indicates which minibinder is fused to each component in each bifaceted nanoparticle. **e**, Representative flow cytometry plots showing the colocalization of IL-2Rβ-coated Nile Red and 4-1BB-coated purple polystyrene particles by functionalized bifaceted nanoparticles. **f**, Quantitation of colocalization detected by flow cytometry. Each data point represents the mean of two technical replicates across three independent biological replicates ($n = 3$). Each bar depicts the mean value of the group, and the error bars depict the standard deviation. Statistical significance was calculated via paired one-way analysis of variance with Geisser–Greenhouse correction followed by Tukey's multiple comparisons test, with individual variances computed for each comparison. Exact P values are reported in the plot. **g**, Representative fluorescence microscopy images showing the colocalization of IL-2Rβ-coated Nile Red and 4-1BB-coated purple polystyrene particles by functionalized bifaceted nanoparticles. The percentage of colocalized beads observed across 25 independent fields of view is displayed in the top-right corner of each image. Scale bar, 60 µm.

generalization of our previously described dock-and-design approach to a wide variety of symmetric architectures[5,19,20,22,33,34,51,52], our approach is not limited to pD5 architectures and, in principle, could be used to design assemblies with pseudo-D_2, pseudo-D_3 or any other dihedral symmetry.

This study also presents, to our knowledge, one of the first methods capable of precisely tuning the structures of designed self-assembling proteins. Most design methods so far have aimed at the more achievable goal of generating single, well-defined target structures due to the sheer complexity of designing novel protein assemblies[5,19–22,34,35,45,51–59]. Nevertheless, designing protein nanomaterials with tunable structures has been a long-standing goal with many potential applications. For example, we exploited the modularity and extensibility of coiled coils to show that varying the antigen–antigen spacing on protein nanoparticle immunogens influences their immunogenicity[60]. Recently, a 'copy–paste' approach to precisely and systematically alter the structures of protein assemblies built from twistless repeat protein building blocks was reported[56]. Both these methods are remarkable for their simplicity,

but are strictly limited to specific types of regularly repeating protein building block: coiled coils and twistless repeat proteins, respectively. Here we took the opposite approach: we achieved precise and systematic control over nanoparticle morphology by leveraging recent advances in artificial-intelligence-based protein structure prediction and design[35,37,45] to create bespoke subunits of the desired sizes and shapes. We obtained multiple hits for all five extended architectures by experimentally screening ten or fewer candidates, a success rate that compares favourably with those observed historically for designing new self-assembling proteins. Combined with ref. 34, our results show that this strategy for fine tuning the structures of self-assembling protein complexes—inpainting between existing protein–protein interfaces arranged in space—should generalize to any symmetric or asymmetric architecture and enable the accurate design of a wide variety of custom self-assembling protein complexes.

We demonstrated the potential utility of the bifaceted nanoparticles by displaying different protein minibinders on each face and using them to specifically colocalize beads coated with two distinct receptor proteins. This required altering the tertiary structure of the nanoparticle subunits so that they had exterior-facing N termini for minibinder display. A similar RFdiffusion–ProteinMPNN–AF2 pipeline, here incorporating block adjacency, again proved successful, yielding two successful designs out of the ten tested and demonstrated another level of control over the structure of designed protein assemblies. We note that even though we only displayed minibinders on the B subunits, all six of the subunits in the bifaceted $(ABC)_5$–$(ABD)_5$ nanoparticles reported here are uniquely addressable. This property derives not only from the well-defined bifaceted architecture of the $(ABC)_5$–$(ABD)_5$ assemblies but also from their hierarchical assembly in vitro. That is, the separate assembly of the $(ABC)_5$ and $(ABD)_5$ components enabled the B subunits on each side to be genetically distinct or independently functionalized. We exploited this property to display different protein minibinders on each face and colocalize receptor-coated beads. Together with the precise structural control afforded by our design approach, this proof of principle demonstrates the potential of computationally designed bifaceted nanoparticles to colocalize distinct biological entities at prescribed distances.

Online content

Any methods, additional references, Nature Portfolio reporting summaries, source data, extended data, supplementary information, acknowledgements, peer review information; details of author contributions and competing interests; and statements of data and code availability are available at https://doi.org/10.1038/s41563-025-02295-7.

References

1. Goodsell, D. S. & Olson, A. J. Structural symmetry and protein function. *Annu. Rev. Biophys. Biomol. Struct.* **29**, 105–153 (2000).
2. Alberts, B. The cell as a collection of protein machines: preparing the next generation of molecular biologists. *Cell* **92**, 291–294 (1998).
3. Lai, Y.-T., King, N. P. & Yeates, T. O. Principles for designing ordered protein assemblies. *Trends Cell Biol.* **22**, 653–661 (2012).
4. Khmelinskaia, A., Wargacki, A. & King, N. P. Structure-based design of novel polyhedral protein nanomaterials. *Curr. Opin. Microbiol.* **61**, 51–57 (2021).
5. Ueda, G. et al. Tailored design of protein nanoparticle scaffolds for multivalent presentation of viral glycoprotein antigens. *eLife* **9**, e57659 (2020).
6. Brouwer, P. J. M. et al. Enhancing and shaping the immunogenicity of native-like HIV-1 envelope trimers with a two-component protein nanoparticle. *Nat. Commun.* **10**, 4272 (2019).
7. Bruun, T. U. J., Andersson, A.-M. C., Draper, S. J. & Howarth, M. Engineering a rugged nanoscaffold to enhance plug-and-display vaccination. *ACS Nano* **12**, 8855–8866 (2018).
8. Boyoglu-Barnum, S. et al. Quadrivalent influenza nanoparticle vaccines induce broad protection. *Nature* **592**, 623–628 (2021).
9. Cohen, A. A. et al. Mosaic nanoparticles elicit cross-reactive immune responses to zoonotic coronaviruses in mice. *Science* **371**, 735–741 (2021).
10. Walls, A. C. et al. Elicitation of potent neutralizing antibody responses by designed protein nanoparticle vaccines for SARS-CoV-2. *Cell* **183**, 1367–1382.e17 (2020).
11. Marcandalli, J. et al. Induction of potent neutralizing antibody responses by a designed protein nanoparticle vaccine for respiratory syncytial virus. *Cell* **176**, 1420–1431.e17 (2019).
12. Liu, Y., Huynh, D. T. & Yeates, T. O. A 3.8 Å resolution cryo-EM structure of a small protein bound to an imaging scaffold. *Nat. Commun.* **10**, 1864 (2019).
13. Liu, Y., Gonen, S., Gonen, T. & Yeates, T. O. Near-atomic cryo-EM imaging of a small protein displayed on a designed scaffolding system. *Proc. Natl Acad. Sci. USA* **115**, 3362–3367 (2018).
14. Castells-Graells, R. et al. Cryo-EM structure determination of small therapeutic protein targets at 3 Å-resolution using a rigid imaging scaffold. *Proc. Natl Acad. Sci. USA* **120**, e2305494120 (2023).
15. McConnell, S. A. et al. Designed protein cages as scaffolds for building multienzyme materials. *ACS Synth. Biol.* **9**, 381–391 (2020).
16. Divine, R. et al. Designed proteins assemble antibodies into modular nanocages. *Science* **372**, eabd9994 (2021).
17. Lutz, I. D. et al. Top-down design of protein architectures with reinforcement learning. *Science* **380**, 266–273 (2023).
18. Mohan, K. et al. Topological control of cytokine receptor signaling induces differential effects in hematopoiesis. *Science* **364**, eaav7532 (2019).
19. King, N. P. et al. Computational design of self-assembling protein nanomaterials with atomic level accuracy. *Science* **336**, 1171–1174 (2012).
20. King, N. P. et al. Accurate design of co-assembling multi-component protein nanomaterials. *Nature* **510**, 103–108 (2014).
21. Hsia, Y. et al. Correction: corrigendum: design of a hyperstable 60-subunit protein icosahedron. *Nature* **540**, 150 (2016).
22. Bale, J. B. et al. Accurate design of megadalton-scale two-component icosahedral protein complexes. *Science* **353**, 389–394 (2016).
23. Wukovitz, S. W. & Yeates, T. O. Why protein crystals favour some space-groups over others. *Nat. Struct. Biol.* **2**, 1062–1067 (1995).
24. Kibler, R. D. et al. Design of pseudosymmetric protein hetero-oligomers. *Nat. Commun.* **15**, 10684 (2024).
25. Lee, S. et al. Four-component protein nanocages designed by programmed symmetry breaking. *Nature* https://doi.org/10.1038/s41586-024-07814-1 (2024).
26. Dowling, Q. M. et al. Hierarchical design of pseudosymmetric protein nanocages. *Nature* https://doi.org/10.1038/s41586-024-08360-6 (2024).
27. Zhang, X., Fu, Q., Duan, H., Song, J. & Yang, H. Janus nanoparticles: from fabrication to (bio)applications. *ACS Nano* **15**, 6147–6191 (2021).
28. Huehls, A. M., Coupet, T. A. & Sentman, C. L. Bispecific T-cell engagers for cancer immunotherapy. *Immunol. Cell Biol.* **93**, 290–296 (2015).
29. Li, X. et al. Preparation and application of Janus nanoparticles: recent development and prospects. *Coord. Chem. Rev.* **454**, 214318 (2022).
30. Zeng, Y. C. et al. Fine tuning of CpG spatial distribution with DNA origami for improved cancer vaccination. *Nat. Nanotechnol.* **19**, 1055–1065 (2024).
31. Jin, H., Cui, J. & Zhan, W. Enzymatic Janus liposome micromotors. *Langmuir* **39**, 4198–4206 (2023).

32. Lee, J., Sands, I., Zhang, W., Zhou, L. & Chen, Y. DNA-inspired nanomaterials for enhanced endosomal escape. *Proc. Natl Acad. Sci. USA* **118**, e2104511118 (2021).
33. Hsia, Y. et al. Design of a hyperstable 60-subunit protein icosahedron. *Nature* **535**, 136–139 (2016).
34. Wang, J. Y. J. et al. Improving the secretion of designed protein assemblies through negative design of cryptic transmembrane domains. *Proc. Natl Acad. Sci. USA* **120**, e2214556120 (2023).
35. Dauparas, J. et al. Robust deep learning-based protein sequence design using ProteinMPNN. *Science* **378**, 49–56 (2022).
36. Lee, S. et al. Four-component protein nanocages designed by programmed symmetry breaking. *Nature* **638**, 546–552 (2025).
37. Jumper, J. et al. Highly accurate protein structure prediction with AlphaFold. *Nature* **596**, 583–589 (2021).
38. Grueninger, D. et al. Designed protein-protein association. *Science* **319**, 206–209 (2008).
39. Garcia-Seisdedos, H., Empereur-Mot, C., Elad, N. & Levy, E. D. Proteins evolve on the edge of supramolecular self-assembly. *Nature* **548**, 244–247 (2017).
40. Carr, K. D. et al. Protein identification using cryo-EM and artificial intelligence guides improved sample purification. *J. Struct. Biol. X* **11**, 100120 (2025).
41. Young, G. et al. Quantitative mass imaging of single biological macromolecules. *Science* **360**, 423–427 (2018).
42. Velas, L. et al. Three-dimensional single molecule localization microscopy reveals the topography of the immunological synapse at isotropic precision below 15 nm. *Nano Lett.* **21**, 9247–9255 (2021).
43. Kirichenko, E. Y., Skatchkov, S. N. & Ermakov, A. M. Structure and functions of gap junctions and their constituent connexins in the mammalian CNS. *Biochem. Moscow Suppl. Ser. A* **15**, 107–119 (2021).
44. Karatekin, E. et al. A 20-nm step toward the cell membrane preceding exocytosis may correspond to docking of tethered granules. *Biophys. J.* **94**, 2891–2905 (2008).
45. Watson, J. L. et al. De novo design of protein structure and function with RFdiffusion. *Nature* **620**, 1089–1100 (2023).
46. Silva, D.-A. et al. De novo design of potent and selective mimics of IL-2 and IL-15. *Nature* **565**, 186–191 (2019).
47. Cao, L. et al. De novo design of picomolar SARS-CoV-2 miniprotein inhibitors. *Science* **370**, 426–431 (2020).
48. Gloegl, M. et al. Target-conditioned diffusion generates potent TNFR superfamily antagonists and agonists. *Science* **386**, 1154–1161 (2024).
49. Dowling, Q. M. et al. Hierarchical design of pseudosymmetric protein nanocages. *Nature* **638**, 553–561 (2025).
50. Sosa, S. et al. Asymmetric bifunctional protein nanoparticles through redesign of self-assembly. *Nanoscale Adv.* **1**, 1833–1846 (2019).
51. Yang, E. C. et al. Computational design of non-porous pH-responsive antibody nanoparticles. *Nat. Struct. Mol. Biol.* **31**, 1404–1412 (2024).
52. Sheffler, W. et al. Fast and versatile sequence-independent protein docking for nanomaterials design using RPXDock. *PLoS Comput. Biol.* **19**, e1010680 (2023).
53. Padilla, J. E., Colovos, C. & Yeates, T. O. Nanohedra: using symmetry to design self assembling protein cages, layers, crystals, and filaments. *Proc. Natl Acad. Sci. USA* **98**, 2217–2221 (2001).
54. de Haas, R. J. et al. Rapid and automated design of two-component protein nanomaterials using ProteinMPNN. *Proc. Natl Acad. Sci. USA* **121**, e2314646121 (2024).
55. Meador, K. et al. A suite of designed protein cages using machine learning and protein fragment-based protocols. *Structure* **32**, 751–765.e11 (2024).
56. Huddy, T. F. et al. Blueprinting extendable nanomaterials with standardized protein blocks. *Nature* **627**, 898–904 (2024).
57. Lai, Y.-T. et al. Structure of a designed protein cage that self-assembles into a highly porous cube. *Nat. Chem.* **6**, 1065–1071 (2014).
58. Hoffnagle, A. M. & Tezcan, F. A. Atomically accurate design of metalloproteins with predefined coordination geometries. *J. Am. Chem. Soc.* **145**, 14208–14214 (2023).
59. Wicky, B. I. M. et al. Hallucinating symmetric protein assemblies. *Science* **378**, 56–61 (2022).
60. Ellis, D. et al. Antigen spacing on protein nanoparticles influences antibody responses to vaccination. *Cell Rep.* **42**, 113552 (2023).

Methods

Docking

From the PDB file containing $Crown_{C5}$-1, which had its five-fold rotational symmetry axis aligned to the *z* axis, we removed all but three chains of one ABC heterotrimer and truncated the C component by 1–4 helices. Because RPXdock is limited to single-chain inputs, for each instance of the heterotrimer with the truncated C component, we connected amino acid residues of all the three chains of the heterotrimers into one chain and saved as a new PDB. These PDB structures were used as the input files for docking into D5_5 by restricting sampling to rotation and translation along the *z* axis using RPXdock[52] (https://github.com/willsheffler/rpxdock). The top scoring and the output with the highest shape compatibility was taken for further design.

Asymmetric interface design

The design of an asymmetrical C–D interface was carried out using the deep learning-based protein sequence design software ProteinMPNN (https://github.com/dauparas/ProteinMPNN). We used ProteinMPNN without biases, ProteinMPNN with adding biases to specific amino acids per residue position and multistate ProteinMPNN. For each method, 100 sequences were designed across different temperatures (0.1, 0.2, 0.4, 0.5, 0.6, 0.8 and 1.0). In the ProteinMPNN with bias per residue position approach, we increased the likelihood of specific amino acids occupying predefined positions using a biasing script (https://github.com/dauparas/ProteinMPNN/blob/main/helper_scripts/make_bias_per_res_dict.py) with a small modification. This script normally favours certain amino acids at specific positions in one chain and disfavouring them in another chain. We modified it to apply positive biases for both chains to increase the probability of the desired amino acids being incorporated on a predefined side. Specifically, we categorized the amino acids S, T, N, Q, V, I and L as small; F, Y and W as bulky; D and E as negatively charged; and R, H and K as positively charged. We biased amino acids in three ways. In the 'charges' approach, we favoured positively charged amino acids on one side and negatively charged on the other side. In the 'clashes' approach, we favoured small amino acids on one side and bulky on the other side. In 'charges-clashes', we favoured positively charged and bulky amino acids on one side and negatively charged and small amino acids on the other side. Bias values of 0.1, 0.2, 0.69, 1.1 and 3.9 were used for both sides in each biasing approach, where 0.69 was for two-fold, 1.1 for three-fold and 3.9 for four-fold increase in likelihood to incorporate the desired amino acid. Multistate ProteinMPNN design was performed as previously described[36] using β-values of −1, −0.5 and −0.25.

Extension of the C component using RFdiffusion

Translation of the portion of $(ABC)_5$ cyclic assemblies was done in PyMOL Molecular Graphics System (v. 2.5.8, Schrödinger). For the full structure extension process, we reasoned that extending only one C component is sufficient, given that the C components are organized in C_5 symmetry and there are no neighbouring subunits with which extensions might clash. For easier computing and to streamline the design filtration process, only four helices of the translated portion of the C component and two isolated helices belonging to the C component were used as an input for RFdiffusion. For each extension distance value, we generated 100 backbones using RFdiffusion (https://github.com/RosettaCommons/RFdiffusion). The ranges of amino acids provided for diffusion to generate the backbones within the gaps were as follows: 50–150, 100–250, 150–350 and 250–400 residues for extensions of 25 Å, 50 Å, 75 Å and 100 Å, respectively. For the 50-Å extension with a subsequent 25° rotation, we used a range of 150–350 residues. The range of amino acids needed to fill the gaps was initially estimated visually for the 25-Å extensions, with an allowance of ±50 residues. For subsequent extensions, the range was determined based on AF2 predictions for the successful 25-Å extensions.

Reorienting N termini using RFdiffusion

To reorient the N termini, we used RFdiffusion with block adjacency[45]. Briefly, we started by modifying the Protein Data Bank (PDB) structure of the ABC heterotrimer to mimic the desired structure with the reoriented N terminus. This involved deleting three loops and adding new loops and one helix of the desired length in specific locations, which we treated as separate chains. These modifications were made using PyMOL. The manipulated PDB structure was then used to create an adjacency matrix, which provided information on which helices the newly built helix (using RFdiffusion) should interact with. RFdiffusion was subsequently used to rebuild the new loops and the helix, generating 100 new heterotrimer backbones.

Construction of synthetic genes

All the synthetic genes were purchased from GenScript. They were codon optimized for expression in *E. coli* and cloned into pET29b+ plasmid between NdeI/XhoI sites. Only the A component had 6×His tag on the C terminus for facilitating the IMAC purification of complexes. The C and D components had mScarlet and mNeonGreen fused to the N terminus, respectively, for easier detection by SEC and SDS-PAGE gel.

Protein expression

Then, 100 ng of each plasmid obtained from GenScript was diluted in 20 µl of DNase-free water (Cytiva). Also, 0.5 µl of each plasmid was used for the transformation of 5 µl of BL21(DE3)Star *E. coli* expression strain (Invitrogen) according to the manufacturer's protocol. One bacterial colony was inoculated in 5 ml of Luria Bertani medium containing 100 µg ml^{-1} of kanamycin and grown overnight at 37 °C with shaking at 225 rpm. Then, 1 ml of the overnight culture was transferred to 50 ml of Terrific Broth II media (MP Biomedical, cat. no. MP113046052) supplemented with 100 µg ml^{-1} of kanamycin in 250-ml flasks. Bacteria was grown at 37 °C until the optical density was 0.6–0.8, and then, the protein expression was induced by adding isopropyl β-D-1-thiogalactopyranoside, after which the temperature was decreased to 18 °C. Expression was continued for 20–24 h with shaking at 225 rpm.

IMAC

Here 50-ml cultures were harvested by centrifugation at 4,000*g* for 20 min at 4 °C. Pelleted bacteria were resuspended in 10 ml of lysis buffer (50 mM of Tris pH 8.0, 300 mM of NaCl, 20 mM of imidazole and 10% glycerol). Resuspensions of A, B and C or A, B and D components were mixed and 300 µl of phenylmethanesulfonyl fluoride (100 mM in 20% ethanol) was added to the mixtures. Immediately on adding phenylmethanesulfonyl fluoride, mixtures were sonicated at 65% power for 5 min, with 10 s of ON/OFF pulse. Lysed bacteria were left on ice for 30 min to allow the formation of ABC heterotrimers and $(ABC)_5$ or $(ABD)_5$ cyclic assemblies, and subsequently centrifuged at 14,000*g* for 30 min at 18 °C. Following centrifugation, the supernatant was kept for an additional 30 min at room temperature to ensure the proper assembly of $(ABC)_5$ or $(ABD)_5$ cyclic assemblies. Subsequently, the supernatant was applied to 1 ml of Ni-NTA resin (Qiagen) for gravity chromatography, which was pre-equilibrated with 5 ml of lysis buffer. Columns were washed with 15 ml of wash buffer (50 mM of Tris pH 8.0, 300 mM of NaCl, 40 mM of imidazole and 10% glycerol) and the protein was eluted with 1.7 ml of elution buffer (50 mM of Tris pH 8.0, 300 mM of NaCl, 300 mM of imidazole, 300 mM of EDTA and 10% glycerol). Only the last 1.3 ml of the elution was collected for further purification.

SEC

Here 1.3 ml of the sample obtained by IMAC purification was further purified using a Superose 6 10/300 Increase column (Cytiva) in SEC buffer (50 mM of Tris pH 8.0 and 300 mM of NaCl) with an ÄKTA Pure chromatography system. In addition to 280-nm absorbance, absorbance at 506 nm and 569 nm was followed. On mixing $(ABC)_5$ and $(ABD)_5$

cyclic assemblies, a second SEC purification was performed using the same buffer.

SDS-PAGE

Peak fractions of cyclic assemblies and D_5 assemblies were analysed by SDS-PAGE electrophoresis. Here 1–5 µg of target protein was resuspended in 2× Laemmli Sample Buffer (Bio-Rad) with adding 1:20 β-mercaptoethanol and 15 µl of the mixture was added onto Any kD Criterion TGX Stain-Free Protein gel (Bio-Rad). Then, 5 µl of Precision Plus Protein Unstained Protein Standards (Bio-Rad) was used and the gels were run at 150 V for ~50 min. Subsequently, the gels were stained with GelCode Blue (Thermo Fisher Scientific) and destained in water. The stained gels were imaged using a Chemidoc XRS+ (Bio-Rad).

nsEM

Here 3 µl of the SEC-purified samples with an approximate concentration of 0.05 mg ml^{-1} was deposited on 10-nm-thick carbon-film-coated 400-mesh copper grids (Electron Microscopy Sciences, CF400-Cu-TH) that was previously glow discharged for 20 s. Subsequently, the grids were stained three times using 2% uranyl formate. Grids were screened using a 120-kV Talos L120C transmission electron microscope. For collecting large datasets to obtain 2D class averages and 3D reconstruction, E. Pluribus Unum (FEI Thermo Scientific) software (v. 2.12.1.2782REL and 3.1.0.4506REL) was used. Data processing was done using CryoSPARC v. 4.2.2, v. 4.4.0 and v. 4.4.1 (Structura Biotechnology). We initially used D_5 symmetry to generate the nsEM models, which then served as the starting point for the subsequent C_1 reconstructions. Fitting of the design models into corresponding density maps was done using ChimeraX[61–63].

DLS

To determine the size and uniformity of the particles, DLS measurements were performed using the sizing and polydispersity method on the Uncle instrument (Unchained Labs). Here 8.8 µl of SEC peak fractions were loaded into the provided glass cuvettes. DLS measurements were measured in triplicate at 25 °C; 10 acquisitions were done, with each measuring 10 s in length. To determine the stability of the nanoparticles, SLS and intrinsic tryptophan fluorescence (presented as the barycentric mean of the emission spectrum) were measured in triplicate at 25 °C, followed by a thermal ramp from 25 °C to 95 °C at a ramp rate of 1.0 °C min^{-1}. Protein concentration (ranging from 0.1 mg ml^{-1} to 0.4 mg ml^{-1}) and buffer conditions were accounted for in the software. Data were processed using Uncle Analysis software (v. 6.01.0.0).

MP

All the MP measurements were carried out on a TwoMP Auto mass photometer using the AcquireMP software (v. 2024 R1.1, Refeyn). Proteins were diluted to ~20 nM at least an hour before measurement in a flat-bottom 96-well polypropylene plate (Greiner). After centring the laser over a well on a 24-well gasket on commercially precleaned slides (Refeyn), 5 µl of buffer (50 mM of Tris and 300 mM of NaCl, pH 8) was deposited into the well using the automated fluid-handling system and used for finding focus using the drop dilution method. After the focus was found, 5 µl of the sample was pipetted into the gasket well and mixed once. One-minute videos were recorded using the normal field of view. Ratiometric contrast values for individual particles in each video were measured and processed into mass distributions with DiscoverMP (v. 2024 R1) using a sample of 20 nM of β-amylase (containing monomers (56 kDa), dimers (112 kDa) and tetramers (224 kDa)) as mass standards. DiscoverMP was used to fit the Gaussian distributions to the experimental mass distributions to calculate the mean mass of the particles.

Cryo-EM sample preparation

To prepare the sample for cryo-EM, 3 µl of the construct at a concentration of 1.5 mg ml^{-1} was pipetted onto a glow-discharged 400-mesh copper ultrathin lacey carbon grid (Electron Microscopy Sciences, LC400-Cu-CC-25). The grid was immediately vitrified by plunge freezing into liquid ethane using a FEI Vitrobot Mk. IV at 22 °C, 100% humidity, with a 7.5-s wait time and a 0.5-s blot time at −1 blot force. Subsequently, the grid was clipped and remained continuously submerged in liquid nitrogen until it was loaded onto the microscope.

Cryo-EM data processing

Using a 300-kV FEI Titan Krios device with a Gatan K3 direct electron detector and a Gatan BioQuantum energy filter, 4,871 videos were collected in SerialEM, utilizing beam shifts to collect 11 videos per stage movement at ×105,000 magnification with a pixel size of 0.843 Å pixel^{-1}. Image stacks were composed of 79 frames at an exposure rate of 0.0505 s per frame with a dose weight of 11.31 e^- A^{-2} s^{-1} and an exposure time of 3.997 s, resulting in a total dose of 45.21 e^- Å^{-2}. All the videos were then imported into CryoSPARC v. 4.4, where all the data processing took place. First, exposures were preprocessed using patch motion correction, patch contrast transfer function estimation and videos were curated, eliminating videos with contrast transfer function fit resolutions below 6 Å and those with average intensities above 472.77. Because of the central cavity and variable diameter of our proteins' minor axis at different view angles, blob picking was unsuccessful. 177 particles were first manually selected, extracted to 800 pixels (952.4 Å) and classified into 2D class averages to generate templates. Two sequential rounds of template picking, extraction to 800 pixels and 2D classification into 150 classes followed, resulting in a final population of 209,004 particles. Those particles were homogeneously refined in C_5 symmetry using an ab initio volume map of this construct previously characterized by nsEM, which was low-pass filtered to 50 Å. Particles were downsampled to 400 pixels to reduce the processing bandwidth before the volume was subsequently refined using non-uniform refinement. Local contrast transfer function refinement was then performed on the particles followed by another round of non-uniform refinement. To finalize the model, one last homogeneous refinement was performed (generating our final half-maps and a global resolution of 4.30 Å), which was then sharpened using a B factor of 239.90 (derived from our homogeneous refinement) sharpened using DeepEMhancer[64] to generate our deposited Coulombic potential map.

Cryo-EM model building

To build our model, the computationally designed model was rigid-body docked into the final cryo-EM map in ChimeraX and was subsequently trimmed to PolyA in Phenix[65,66], and the backbone was relaxed into our volume map using Namdinator[67]. We then manually refined the backbone using ISOLDE[68] in ChimeraX, and Coot[69]. Side chains were trimmed to PolyA and a wwPDB validation service[70,71] report was generated to verify that the model's clashscore and Ramachandran outliers were each zero (Supplementary Table 2). The final structure was deposited in the PDB and Electron Microscopy Data Bank under accession nos. 9DZE and EMD-47327, respectively.

BLI

BLI was performed on Octet R8 (Sartorius). All the biosensors were hydrated in a kinetic buffer (10 mM of HEPES pH 7.4 and 1% w/v of bovine serum albumin (BSA)). Biotinylated human IL-2Rβ (Acro Biosystems, ILB-H82E3) and human 4-1BB (Sino Biological, 10041-H27H-B) were diluted to a concentration of 2.5 µg ml^{-1} in the kinetic buffer and loaded onto streptavidin-coated biosensors (SAForteBio). Complexes were diluted in the kinetic buffer to a concentration of 15 nM and its association was measured for 300 s, followed by a dissociation for 300 s in the kinetic buffer. Data were processed using ForteBio Data Analysis software (v. 9.0.0.10).

Flow cytometry

Here 200 µl of streptavidin-coated fluorescent Nile Red and purple particles with a nominal size of 5.0–7.9 µm (Spherotech) were washed

three times in phosphate-buffered saline (PBS) containing 0.01% Tween 20 and 0.05% BSA according to the manufacturer's protocol with spinning for 30 s at 21,000*g*. After washing, both particle types were resuspended in 250 µl of PBS with 0.01% Tween 20 and 0.05% BSA. Biotinylated human IL-2Rβ (Acro Biosystems, ILB-H82E3) and human 4-1BB (Sino Biological, 10041-H27H-B) were incubated with Nile Red and purple particles, respectively, at a concentration of 10 µg of receptor per 1 mg of Spherotech streptavidin particles, with gentle rotation for 30 min. The particles coated with biotinylated receptors were separated from unbound receptors by centrifugation at 21,000*g* for 30 s, followed by five washes in PBS with 0.01% Tween 20 and 0.05% BSA. On washing, particles were resuspended in 250 µl of PBS with 0.01% Tween 20 and 0.05% BSA. Finally, 1 µl of each particle suspension was further resuspended in 18 µl of PBS with 0.01% Tween 20 and 0.05% BSA, to which 100 µl of the sample was added. The mixture was incubated at room temperature for 30 min and colocalization events were acquired using an AttuneNXT flow cytometer (Thermo Fisher). Data files were analysed using FlowJo software (v. 10; BD Biosciences). Statistical analysis was performed using a one-way analysis of variance with Geisser–Greenhouse correction followed by Tukey's multiple comparisons test, with individual variances computed for each comparison.

Fluorescence microscopy

Coating streptavidin-coated fluorescent Nile Red and purple particles with biotinylated human IL-2Rβ (Acro Biosystems, ILB-H82E3) and human 4-1BB (Sino Biological, 10041-H27H-B) was performed following the same procedure as the flow cytometry experiments. Here 1 µl of each particle suspension was resuspended in 18 µl of PBS containing 0.01% Tween 20 and 0.05% BSA. Then, 4 µl of this mixture was incubated with 20 µl of the sample at room temperature for 30 min. Subsequently, the mixture was placed in a glass-bottom 18-well ibidi slide and the particles were allowed to settle for 10 min before imaging. Images were acquired on an IN Cell Analyser 2500HS microscope using a Nikon Plan Apo, CFI/60 ×20 objective with a numerical aperture of 0.75. Fluorescent particles were excited using light-emitting diodes emitting at 473 nm and 575 nm each with 10-ms exposure times. Emission was collected through bandpass filters centred at 525 (±24) nm and 623 (±12) nm, respectively. Each sample was imaged in 25 separate fields of view for quantification. Briefly, quantification was carried out using a custom Python script (Python v. 3.12.8) that segmented fluorescent particles in each channel and then, using one channel as a reference, measured the distance between each identified fluorescent particle and all the fluorescent particles of the opposite colour. Only fluorescent particles with a centroid-to-centroid separation distance of less than 7.5 µm (representing roughly twice the radius of the fluorescent particle) were kept as positive hits for fluorescent particle interaction. Per-cent fluorescent particle interactions were then determined by dividing the interacting fluorescent particles by the total fluorescent particle count for each channel in each image.

Data availability

The cryo-EM density map of pD5-14 has been deposited in the Electron Microscopy Data Bank (https://www.ebi.ac.uk/pdbe/emdb/) under accession no. EMD-47327. The atomic coordinates of pD5-14 have been deposited in the PDB (https://www.rcsb.org) under accession no. 9DZE. All other data are available in the Article and its Supplementary Information, or available from the corresponding author upon request. Requests for resources or reagents should be directed to and will be fulfilled by the corresponding author. Source data are provided with this paper.

Code availability

The source code for RPXdock, ProteinMPNN and RFdiffusion are available via GitHub at https://github.com/willsheffler/rpxdock, https://github.com/dauparas/ProteinMPNN and https://github.com/RosettaCommons/RFdiffusion, respectively.

References

61. Pettersen, E. F. et al. UCSF ChimeraX: structure visualization for researchers, educators, and developers. *Protein Sci.* **30**, 70–82 (2021).
62. Meng, E. C. et al. UCSF ChimeraX: tools for structure building and analysis. *Protein Sci.* **32**, e4792 (2023).
63. Goddard, T. D. et al. UCSF ChimeraX: meeting modern challenges in visualization and analysis. *Protein Sci.* **27**, 14–25 (2018).
64. Sanchez-Garcia, R. et al. DeepEMhancer: a deep learning solution for cryo-EM volume post-processing. *Commun. Biol.* **4**, 874 (2021).
65. Liebschner, D. et al. Macromolecular structure determination using X-rays, neutrons and electrons: recent developments in Phenix. *Acta Cryst.* **D75**, 861–877 (2019).
66. Davis, I. W. et al. MolProbity: all-atom contacts and structure validation for proteins and nucleic acids. *Nucleic Acids Res.* **35**, W375–W383 (2007).
67. Kidmose, R. T. et al. Namdinator—automatic molecular dynamics flexible fitting of structural models into cryo-EM and crystallography experimental maps. *IUCrJ* **6**, 526–531 (2019).
68. Croll, T. I. ISOLDE: a physically realistic environment for model building into low-resolution electron-density maps. *Acta Cryst.* **D74**, 519–530 (2018).
69. Emsley, P., Lohkamp, B., Scott, W. G. & Cowtan, K. Features and development of Coot. *Acta Cryst.* **D66**, 486–501 (2010).
70. wwPDB Consortium Protein Data Bank: the single global archive for 3D macromolecular structure data. *Nucleic Acids Res.* **47**, D520–D528 (2019).
71. Ellis, D. et al. Structure-based design of stabilized recombinant influenza neuraminidase tetramers. *Nat. Commun.* **13**, 1825 (2022).

Acknowledgements

We thank J. Watson and D. Juergens for helpful discussions, Q. Dowling for providing RPXdock scripts, L. Goldschmidt and P. Vecchiato for maintaining the computing resources, K. VanWormer and H. Nunez-Ortega for the wet-laboratory management, and J. Quispe and S. Dickinson for management of the University of Washington cryo-EM facilities. This work was funded by the Bill & Melinda Gates Foundation (INV-043758 to D.B. and N.P.K.), the National Institute of Allergy and Infectious Disease (U54AI170856, 1P01AI167966 and U19AI181881 to N.P.K.), ARPA-H (P023 to D.B. and N.P.K.), the Howard Hughes Medical Institute (D.B.), the Audacious Project at the Institute for Protein Design (D.B. and N.P.K.), the Shurl and Kay Curci Foundation (H.E.E.), the Swedish Research Council (S.O.) and the Open Philanthropy Project Improving Protein Design Fund (D.B.).

Author contributions

S.R. and N.P.K. conceptualized the study and devised the design strategies. S.R. designed the nanomaterials and purified all the protein nanomaterials. S.R., K.D.C. and R.S. characterized and collected the nsEM data of the protein nanomaterials. S.R. analysed and processed the nsEM data. K.D.C., C.W. and A.J.B. collected, analysed and processed the cryo-EM data. R.D.K. performed the MP measurements. S.R. performed the SDS-PAGE analysis and DLS measurements. J.-H.C. and M.R.T. performed the BLI measurements. S.R. prepared the samples for fluorescence microscopy and flow cytometry. J. Decarreau performed the fluorescence microscopy and analysed the data. S.R. and S.O. performed the flow cytometry and analysed the data. M.G. provided the sequence for the 4-1BB minibinder. S.L. provided the sequence for $Crown_{C5}$-1. H.E.E. and J. Dauparas edited part of the ProteinMPNN helper scripts. S.R. and N.P.K. wrote and revised the manuscript with input from all authors.

Competing interests
The authors declare no competing interests.

Additional information
Extended data is available for this paper at https://doi.org/10.1038/s41563-025-02295-7.

Supplementary information The online version contains supplementary material available at https://doi.org/10.1038/s41563-025-02295-7.

Correspondence and requests for materials should be addressed to Neil P. King.

Peer review information *Nature Materials* thanks Guto Rhys, Shuguang Zhang and the other, anonymous, reviewer(s) for their contribution to the peer review of this work.

https://doi.org/10.1038/s41563-025-02295-7

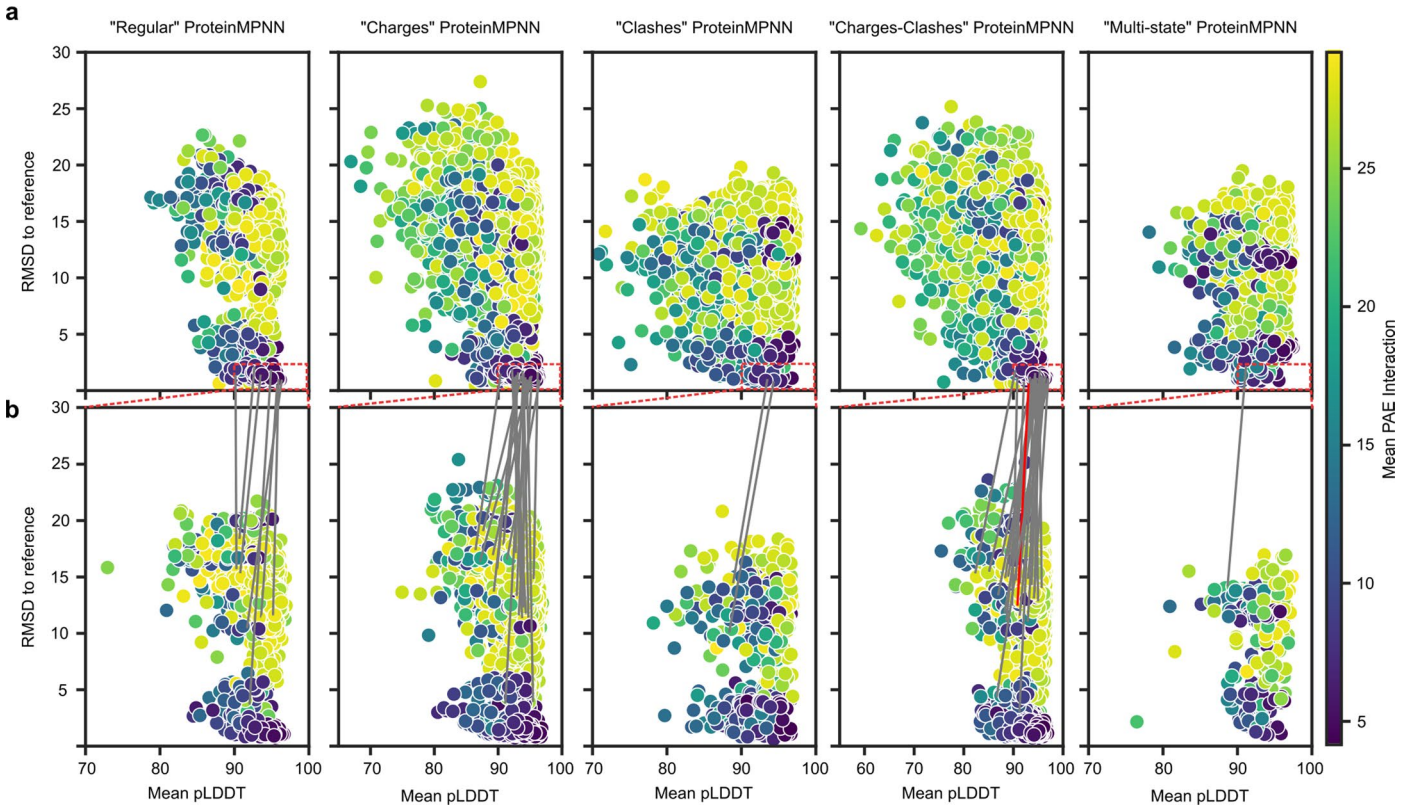

Extended Data Fig. 1 | AF2 structure prediction metrics of designed asymmetric C-D interface. a, AF2 metrics for the asymmetric C-D interface designs. The structures of the five C-terminal helices of the C and D subunits, comprising the designed interface, were predicted and pLDDT and pAE were plotted against RMSD to the computational design models (post-ProteinMPNN). Metrics for designs from each of the five ProteinMPNN strategies used to design asymmetric interfaces are shown separately. Each point represents a prediction from one of five AF2 models used to evaluate each design. Designs that passed the first round of filtering and were evaluated for off-target homotypic interface formation are boxed in red. **b**, AF2 metrics for off-target C-C or D-D interface formation using sequences that passed the first round of filtering. Only data corresponding to the best (that is, lowest mean pAE interaction) off-target prediction for each design are shown. Gray lines connect data points for designs that were predicted to form the on-target C-D interface (**a**) and predicted to not form off-target C-C or D-D interfaces (**b**). The red line connects the on-target and off-target data points for pD5-14, which was experimentally verified to form exclusively $(ABC)_5$-$(ABD)_5$ complexes.

https://doi.org/10.1038/s41563-025-02295-7

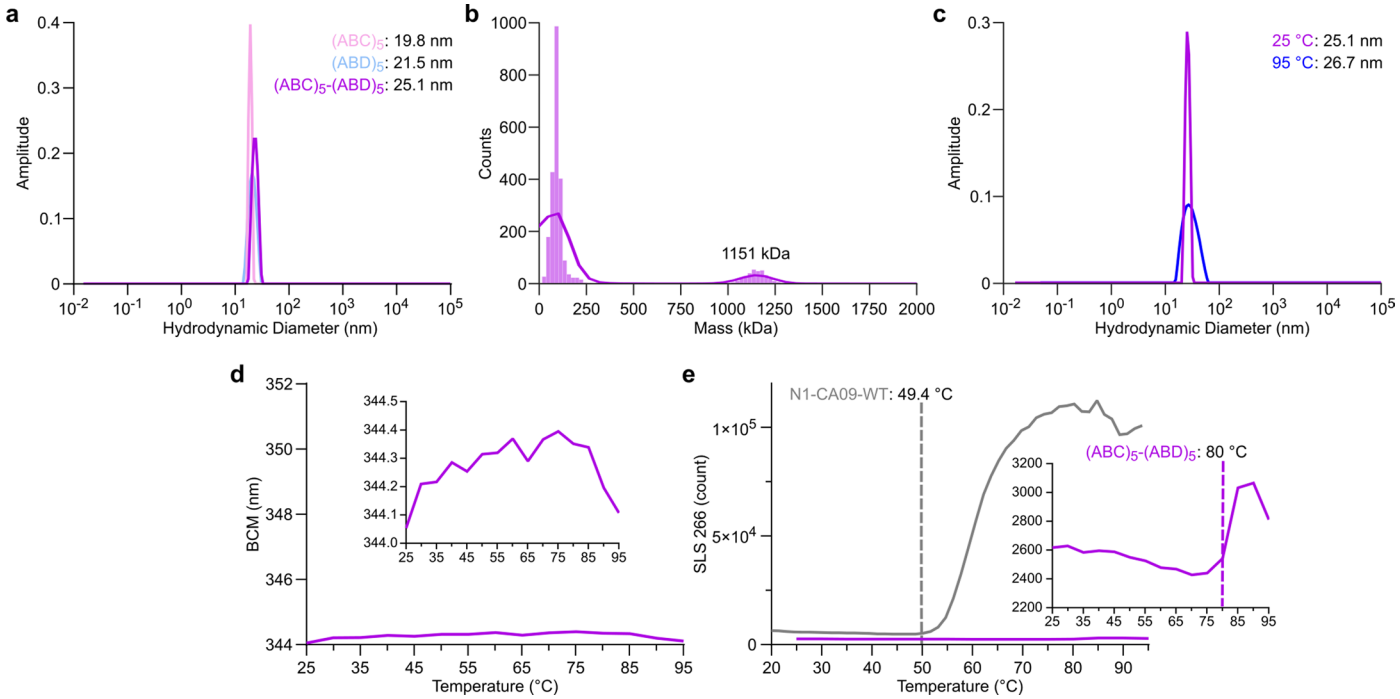

Extended Data Fig. 2 | Size distribution and thermal stability of pD5-14 bifaceted nanoparticles. a, DLS and measured hydrodynamic diameters of pD5-14 $(ABC)_5$, $(ABD)_5$, and $(ABC)_5$-$(ABD)_5$. **b**, Mass photometry of pD5-14 $(ABC)_5$ + $(ABD)_5$, showing an observed mass of 1151 kDa. The expected mass for the 30-subunit assembly is 1252 kDa. **c**, DLS measurements of pD5-14 $(ABC)_5$-$(ABD)_5$ at 25 °C and 95 °C. **d**, Nano differential scanning fluorimetry of $(ABC)_5$-$(ABD)_5$, plotted as the barycentric mean (BCM) of the emission spectrum during heating from 25–95 °C. The y axis spans the range of BCM values typically observed during protein denaturation, while the inset zooms in on the y axis to show the details of the data. **e**, Evaluation of thermal aggregation of $(ABC)_5$-$(ABD)_5$, measured by scattering intensity at 266 nm during heating from 25–95 °C. Thermal aggregation of an N1 influenza neuraminidase ectodomain (N1-CA09-WT)[74] is shown for comparison, while the inset zooms in on the y axis to show the details of the data $(ABC)_5$-$(ABD)_5$. Aggregation temperatures, as determined by UNcle Analysis Software, are indicated by dashed lines. Each panel contains a representative example of at least 3 independent measurements from at least 2 different sample purifications.

https://doi.org/10.1038/s41563-025-02295-7

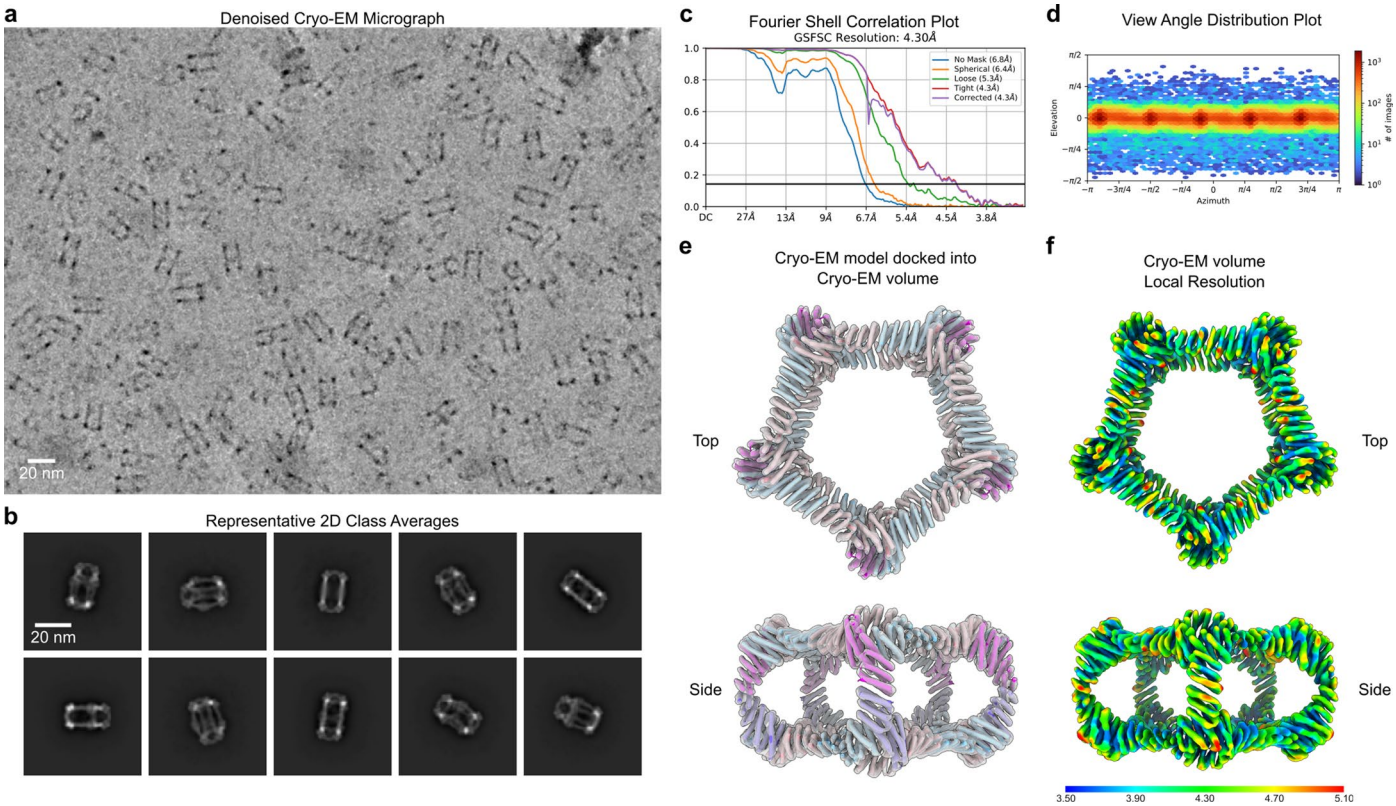

Extended Data Fig. 3 | Details of cryo-EM data processing. a, Denoised representative cryo-EM micrograph. **b**, Representative 2D class averages with scale bar showing particles from multiple view angles, exemplifying preference for 'Side' views over 'Top' views. **c**, Fourier Shell Correlation (FSC) plot of volume map, illustrating 4.30 Å resolution estimation at FSC 0.143 cutoff. **d**, View angle distribution plot, demonstrating spatial preference for 'Side' views over 'Top' views. **e**, Cryo-EM model docked into cryo-EM volume. **f**, Local resolution estimation (Å) of cryo-EM volume. Scale bars: 20 nm.

https://doi.org/10.1038/s41563-025-02295-7

Extended Data Fig. 4 | Representative RFdiffusion and AF2 outputs of de novo extensions. a, Backbone structures of ABC heterotrimers output from RFdiffusion for different extension lengths. The images are oriented such that the two C-terminal helices of the C subunit that make up the pseudo-dihedral interface (pink) are at bottom. The de novo extensions that connect the C-terminal helices to the rest of the C subunit are colored gray. RFdiffusion generated diverse structures including both α-helices and β-sheets. **b**, Representative extended ABC heterotrimers that passed AF2 filtering. The *de novo* extensions of passing designs generally had well-packed α-helical repeat structures.

https://doi.org/10.1038/s41563-025-02295-7

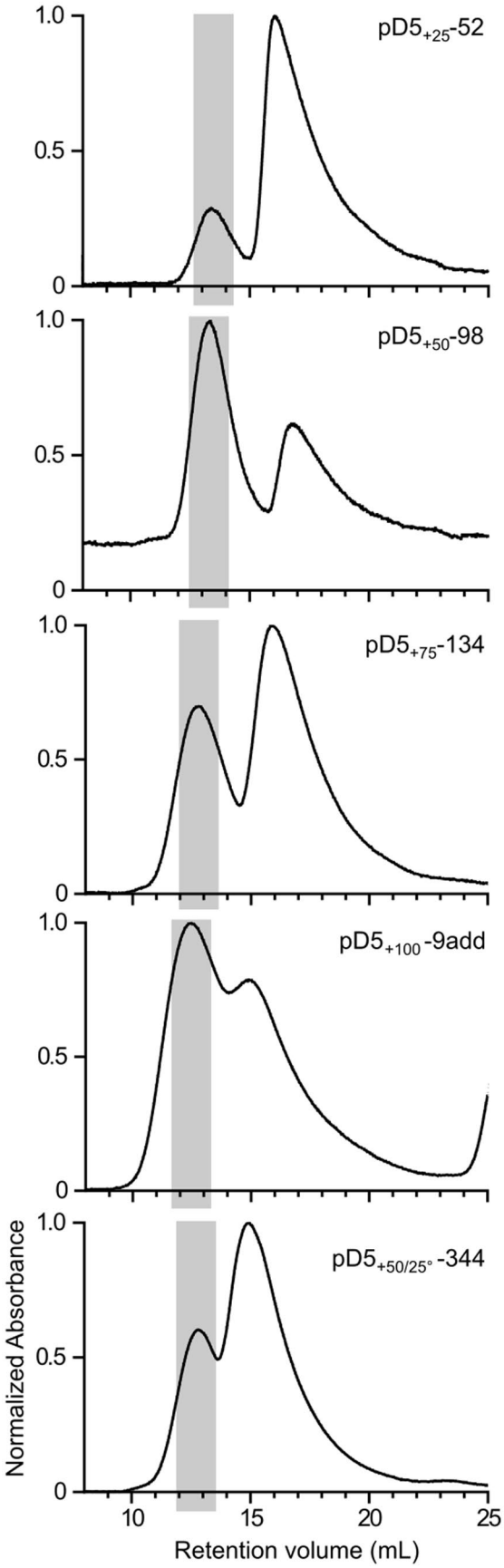

Extended Data Fig. 5 | SEC of extended bifaceted pD5 nanoparticles. Preparative SEC chromatograms are shown for each of the five extended pD5 nanoparticles shown in Fig. 4. The gray rectangles depict the fractions pooled for further characterization.

https://doi.org/10.1038/s41563-025-02295-7

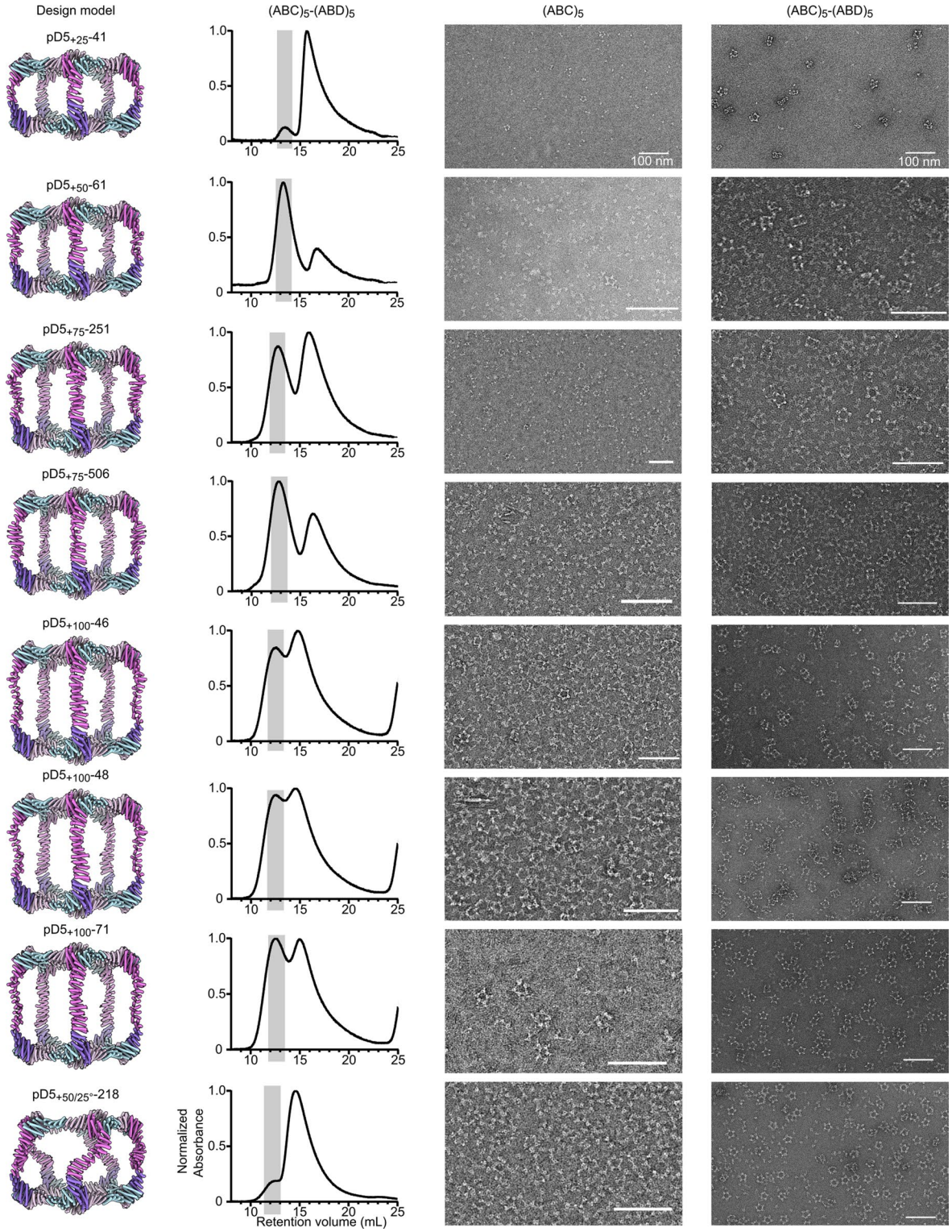

Extended Data Fig. 6 | Experimental characterization of additional extended bifaceted pD5 nanoparticles. *From top to bottom*: Additional assemblies extended by 25, 50, 75, and 100 Å, or extended by 50 Å and rotated by 25°. *From left to right*: computational design models, preparative SEC chromatograms, raw micrographs of $(ABC)_5$, and raw micrographs of $(ABC)_5$-$(ABD)_5$. Scale bars: 100 nm.

https://doi.org/10.1038/s41563-025-02295-7

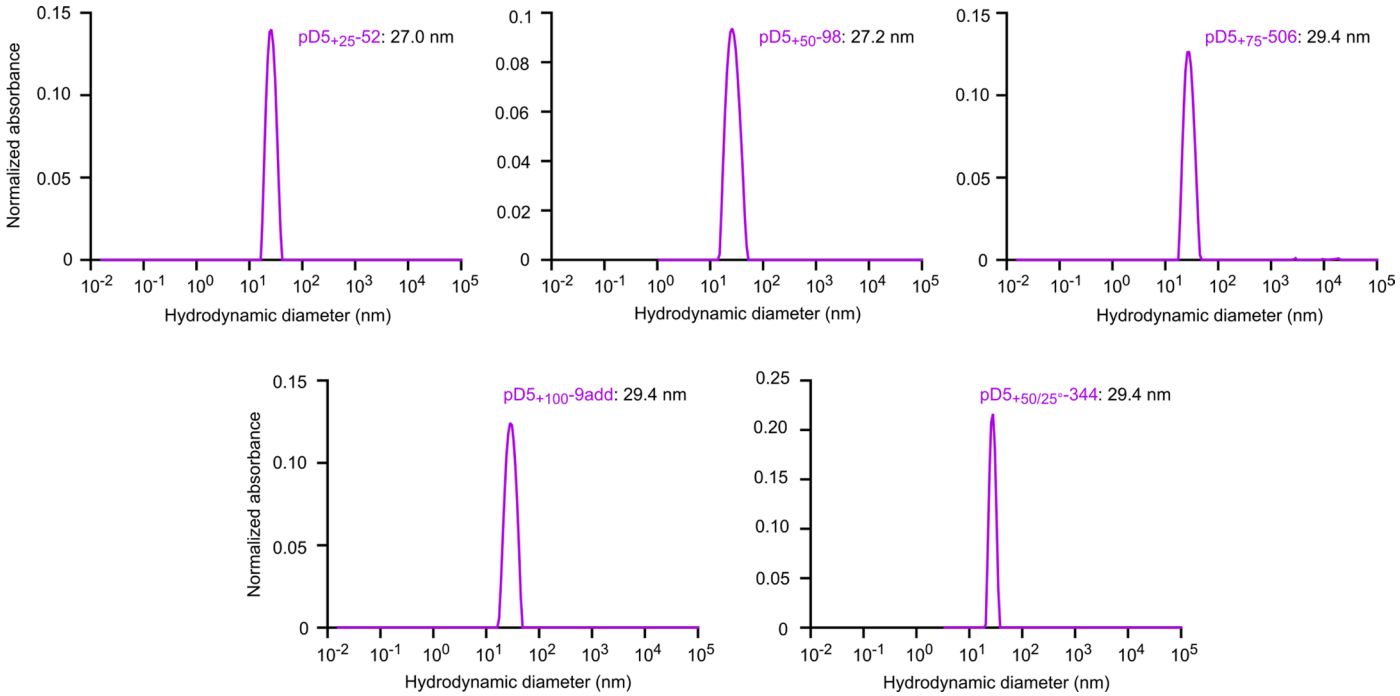

Extended Data Fig. 7 | DLS of SEC-purified extended bifaceted pD5 nanoparticles. DLS and measured hydrodynamic diameters of additional assemblies extended by 25, 50, 75, and 100 Å, or extended by 50 Å and rotated by 25°.

https://doi.org/10.1038/s41563-025-02295-7

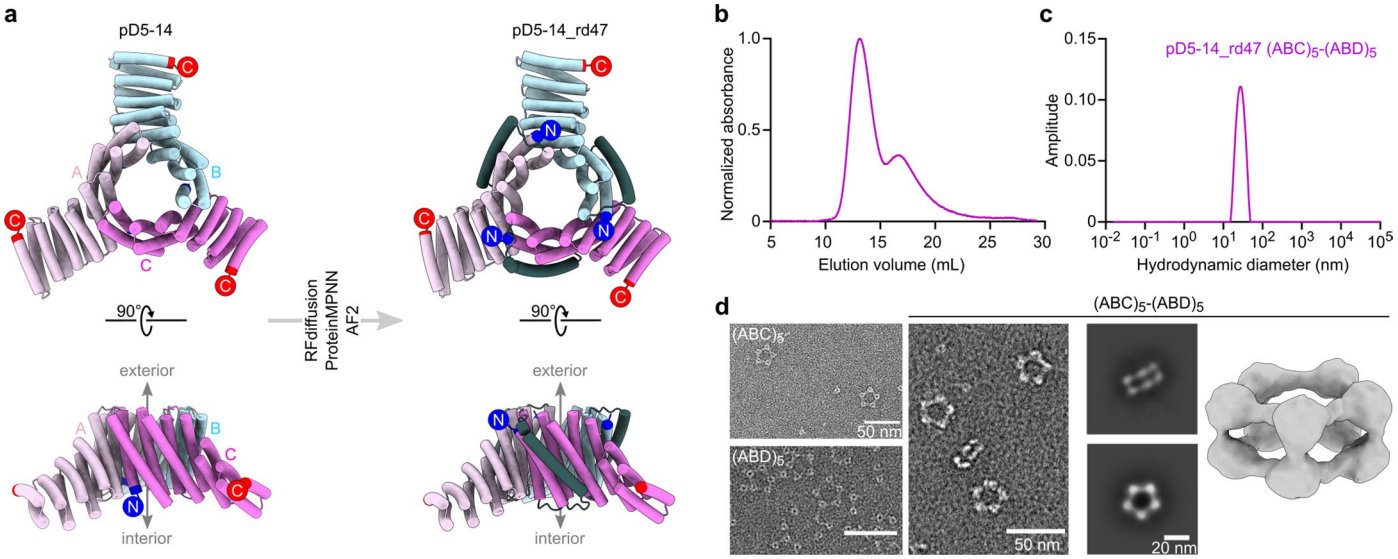

Extended Data Fig. 8 | Experimental characterization of pD5-14_rd47. **a**, Schematic of pD5-14 ABC heterotrimer redesign to generate pD5-14_rd47 ABC heterotrimers with exterior-facing N termini. The newly diffused α-helix is shown in dark gray, and N and C termini are indicated by blue and red circles, respectively. **b**, Preparative SEC chromatogram of pD5-14_rd47. **c**, DLS of SEC-purified pD5-14_rd47 $(ABC)_5$-$(ABD)_5$. **d**, nsEM characterization of pD5-14_rd47. *Left*: Raw micrographs are shown for the $(ABC)_5$ and $(ABD)_5$ components as well as the SEC-purified $(ABC)_5$-$(ABD)_5$ assemblies. *Right*: 2D class averages and a 3D reconstruction of pD5-14_rd47 $(ABC)_5$-$(ABD)_5$. Scale bars: 50 nm (raw micrographs) and 20 nm (2D class averages).

https://doi.org/10.1038/s41563-025-02295-7

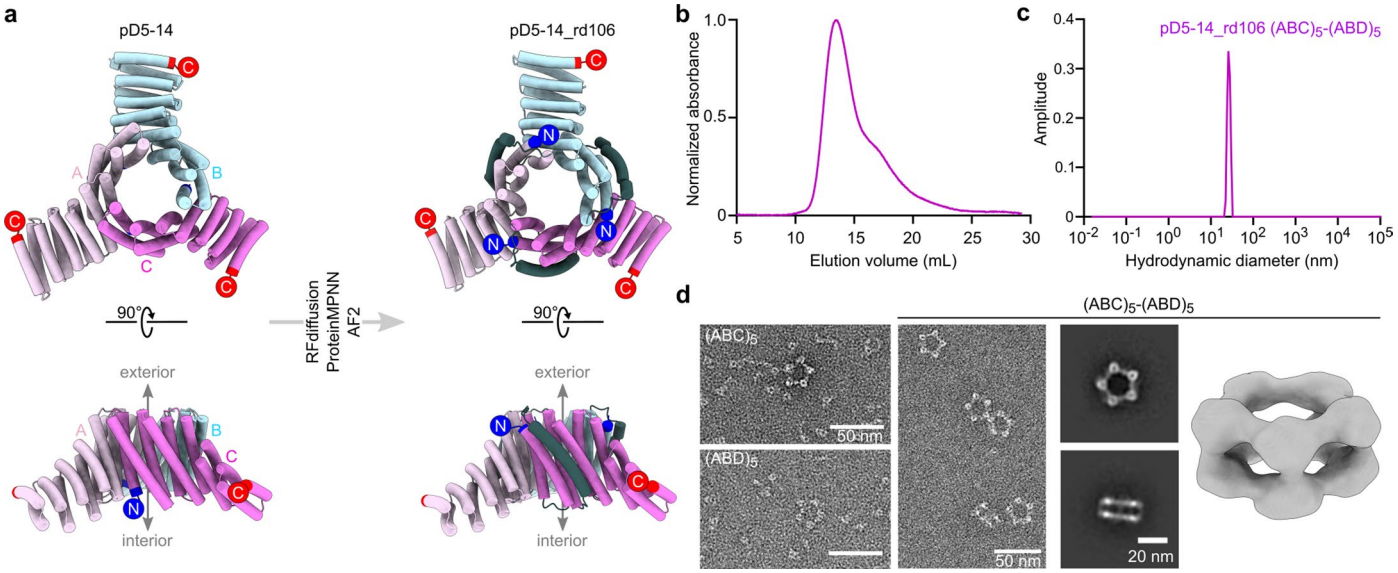

Extended Data Fig. 9 | Characterization of pD5-14_rd106. a, Schematic of pD5-14 ABC heterotrimer redesign to generate pD5-14_rd106 ABC heterotrimers with exterior-facing N termini. The newly diffused α-helix is shown in dark gray, and N and C termini are indicated by blue and red circles, respectively. **b**, Preparative SEC chromatogram of pD5-14_rd106. **c**, DLS of SEC-purified pD5-14_rd106 $(ABC)_5$-$(ABD)_5$. **d**, nsEM characterization of pD5-14_rd106. *Left*: Raw micrographs are shown for the $(ABC)_5$ and $(ABD)_5$ components as well as the SEC-purified $(ABC)_5$-$(ABD)_5$ assemblies. *Right*: 2D class averages and a 3D reconstruction of pD5-14_rd106 $(ABC)_5$-$(ABD)_5$. Scale bars: 50 nm (raw micrographs) and 20 nm (2D class averages).

https://doi.org/10.1038/s41563-025-02295-7

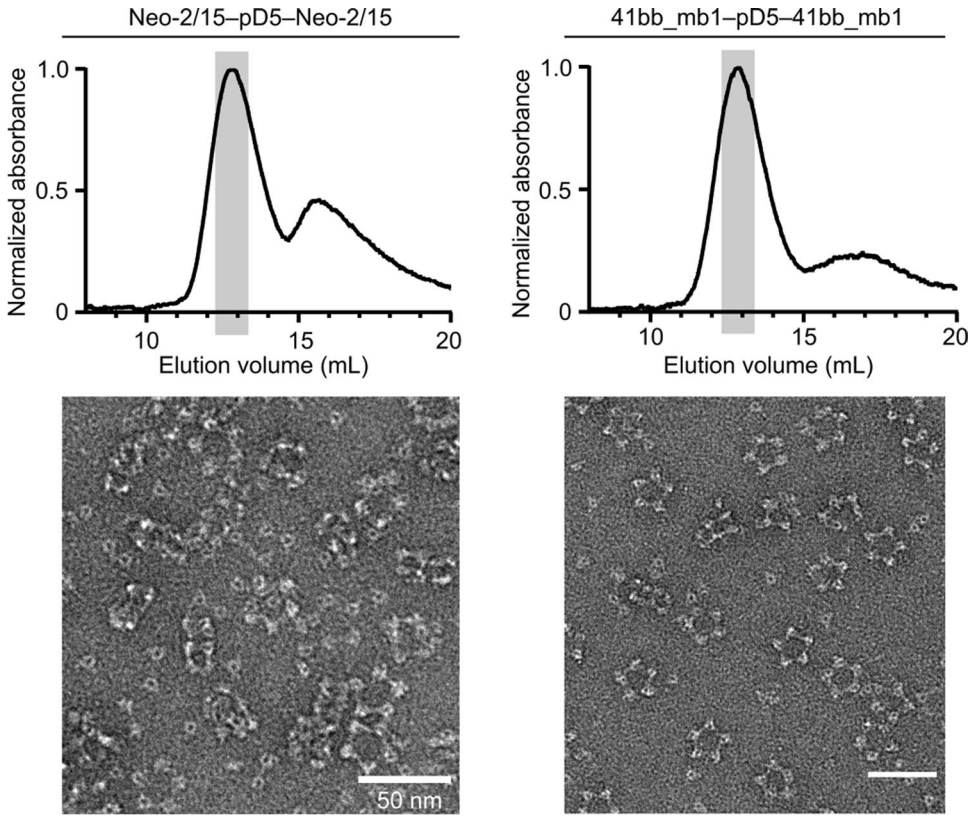

Extended Data Fig. 10 | SEC and nsEM of Neo-2/15–pD5–Neo-2/15 and 41bb_mb1–pD5–41bb_mb1 assemblies. *Top*: Preparative SEC chromatograms of Neo-2/15–pD5–Neo-2/15 and 41bb_mb1–pD5-14–41bb-mb1. The fractions collected for further characterization are marked by gray rectangles. *Bottom*: nsEM raw micrographs of the SEC-purified assemblies. Scale bar: 50 nm for both micrographs.